

1 **Myeloid-specific KDM6B inhibition sensitizes Glioblastoma to PD1 blockade**

2 Sangeeta Goswami<sup>1,2†\*</sup>, Deblina Raychaudhuri<sup>1†</sup>, Pratihtha Singh<sup>1†</sup>, Seanu Meena Natarajan<sup>1†</sup>,  
3 Yulong Chen<sup>3</sup>, Candice Poon<sup>4</sup>, Mercedes Hennessey<sup>1</sup>, Jan Zhang<sup>2</sup>, Swetha Anandhan<sup>2</sup>, Brittany  
4 Parker Kerrigan<sup>4</sup>, Marc D. Macaluso<sup>3</sup>, Zhong He<sup>3</sup>, Sonali Jindal<sup>3</sup>, Frederick F. Lang<sup>4</sup>, Sreyashi  
5 Basu<sup>3</sup>, Padmanee Sharma<sup>1,2,3\*</sup>

6

7 <sup>1</sup>Department of Immunology, The University of Texas MD Anderson Cancer Center, Houston,  
8 Texas. <sup>2</sup>Department of Genitourinary Medical Oncology, The University of Texas MD Anderson  
9 Cancer Center, Houston, Texas. <sup>3</sup>Immunotherapy Platform, The University of Texas MD  
10 Anderson Cancer Center, Houston, Texas. <sup>4</sup>Department of Neurosurgery, The University of  
11 Texas MD Anderson Cancer Center, Houston, Texas.

12

13 †Contributed equally

14 \*Corresponding authors. Email: [padsharma@mdanderson.org](mailto:padsharma@mdanderson.org), [sgoswami@mdanderson.org](mailto:sgoswami@mdanderson.org)

15

16

17

18

19

20

21

22 **Abstract**

23 Glioblastoma (GBM) tumors are enriched in immune-suppressive myeloid cells and are refractory  
24 to immune checkpoint therapy (ICT). Targeting epigenetic pathways to reprogram the functional  
25 phenotype of immune-suppressive myeloid cells to overcome resistance to ICT remains  
26 unexplored. Single-cell and spatial transcriptomic analyses of human GBM tumors demonstrated  
27 high expression of an epigenetic enzyme - histone 3 lysine 27 demethylase (KDM6B) in intra-  
28 tumoral immune-suppressive myeloid cell subsets. Importantly, myeloid-cell specific *Kdm6b*  
29 deletion enhanced pro-inflammatory pathways and improved survival in GBM tumor-bearing  
30 mice. Mechanistic studies elucidated that the absence of *Kdm6b* enhances antigen-presentation,  
31 interferon response and phagocytosis in myeloid cells by inhibiting mediators of immune  
32 suppression including *Mafb*, *Socs3* and *Sirpa*. Further, pharmacological inhibition of KDM6B  
33 mirrored the functional phenotype of *Kdm6b* deleted myeloid cells and enhanced anti-PD1  
34 efficacy. Thus, this study identified KDM6B as an epigenetic regulator of the functional phenotype  
35 of myeloid cell subsets and a potential therapeutic target to improve response to ICT.

36

37

38

39

40

41

42

43

44 **Main**

45 Immune cells of the myeloid lineage constitute a dominant portion of the tumor immune  
46 microenvironment and demonstrate significant plasticity depending on cues received from the  
47 environment <sup>1,2</sup>. While pro-inflammatory myeloid cells are crucial for mounting an effective anti-  
48 tumor immune response, immune-suppressive myeloid cells are associated with poor prognosis  
49 and therapeutic resistance in multiple cancer types <sup>3-6</sup>. Emerging evidence suggests that immune-  
50 suppressive myeloid cells play a critical role in both primary and adaptive resistance to  
51 immunotherapy <sup>7-11</sup>. Therefore, developing therapeutic strategies to target immune-suppressive  
52 myeloid cells is a critical approach to enhance response to cancer immunotherapy and has been  
53 the focus of intense research for many years <sup>12-14</sup> .

54 Most studies have focussed on depleting intratumoral immune-suppressive myeloid cells,  
55 blocking their trafficking, and targeting individual immune-suppressive pathways to enhance anti-  
56 tumor immunity <sup>15-20</sup>. However, many of these strategies have not been successfully translated to  
57 the clinic partly due to the functional heterogeneity and redundancy of pathways in myeloid cell  
58 subsets. Newer technologies such as single cell RNA sequencing (scRNA seq) further  
59 demonstrated the wide spectrum of functional states attained by each of these subsets based on  
60 signals received from the niche they inhabit <sup>21-25</sup>. This significant plasticity of myeloid cells  
61 highlights the important role of epigenetic regulation of their cell state <sup>26,27</sup>. However, the impact  
62 of epigenetic regulation of intratumoral myeloid cell plasticity on therapeutic resistance remains  
63 largely unexplored.

64 Glioblastoma (GBM) is an aggressive form of brain tumor, highly infiltrated with immune-  
65 suppressive myeloid cells and demonstrates resistance to ICT <sup>28-31</sup>. We have previously shown  
66 the persistence of tumor-associated macrophages (TAMs) in the GBM tumor microenvironment  
67 even after treatment with anti-PD1 therapy <sup>32</sup>. In this study, we aimed to identify epigenetic factors  
68 regulating the functional phenotype of intratumoral myeloid cell subsets in order to reprogram

69 these cells to a pro-inflammatory state thus enhancing anti-tumor immunity and efficacy of ICT.  
70 scRNA seq of GBM tumors resected from patients demonstrated high expression of histone 3  
71 lysine 27 demethylase (KDM6B) in myeloid cell subsets including monocytes, macrophages and  
72 dendritic cells (DCs). Further, spatial transcriptomic analysis of human GBM tumors showed  
73 significant infiltration of *KDM6B* expressing immune-suppressive myeloid cells in the tumor  
74 microenvironment (TME). KDM6B is an epigenetic enzyme that demethylates the repressive  
75 trimethylation mark at histone 3 lysine 27 (H3K27me3) thereby promoting gene transcription<sup>33</sup>.  
76 Importantly, in murine models of GBM, *LysM<sup>cre</sup>KDM6B<sup>fl/fl</sup>* mice carrying *Kdm6b* deletion in myeloid  
77 cells had enhanced pro-inflammatory pathways and improved survival compared with their wild-  
78 type counterparts. Single-cell assay for transposase-accessible chromatin sequencing (scATAC  
79 seq) and chromatin immunoprecipitation followed by sequencing (ChIP seq) demonstrated that  
80 KDM6B directly regulates H3K27me3 enrichment of genes including *Mafb*, *Socs3* and *Sirpa* which  
81 inhibit critical pro-inflammatory pathways such as cytokine production and phagocytosis in  
82 macrophages<sup>19,20,34,35</sup>, providing mechanistic insight into enhanced pro-inflammatory pathways  
83 noted in the absence of *Kdm6b*. Further, pharmacological inhibition of KDM6B could recapitulate  
84 the functional phenotype of *Kdm6b* deleted myeloid cells and improve sensitivity to anti-PD1  
85 therapy in GBM. Together, these findings have provided critical insight into KDM6B-mediated  
86 epigenetic regulation of intratumoral myeloid cell functions. Overall, this study proposes a new  
87 paradigm of targeting the epigenetic machinery to regulate intratumoral myeloid cell plasticity thus  
88 reprogramming them into a pro-inflammatory phenotype to overcome myeloid cell-mediated  
89 resistance to ICT.

90

91 **Single-cell and spatial transcriptomic analyses of human GBM tumors demonstrated**  
92 **selective expression of *KDM6B* in immune-suppressive myeloid cells**

93 We performed scRNA seq of intratumoral *CD45+* cells in GBM tumors resected from patients  
94 (n=5). The patient characteristics are highlighted in Supplementary Table 1. Unsupervised  
95 clustering and uniform manifold approximation and projection (UMAP) analyses revealed distinct  
96 *CD3E+CD4+*T cells (C2), *CD3E+CD4+FOXP3+* regulatory T cells (C14), *CD3E+CD8A+*T cell  
97 (C5,7,9,10,11), *KLRK1+NK* cell (C13), *CD19+CD79+* B cell (C15), and myeloid cell subsets  
98 (C0,1,4,3,6,8,16) (Fig.1A, Extended Data Fig. 1A). Next, to investigate the intratumoral myeloid  
99 cells in human GBM samples in greater detail, we re-clustered myeloid cell populations  
100 characterized by the expression of *CD68* (Fig. 1B). Annotation of each of these individual clusters  
101 (Fig. 1B-C) revealed the presence of three microglial-like clusters (C0,4 and 8), one  
102 *STAB1+LYVE1+DAB2+* brain-associated macrophage cluster (C3), a  
103 *CHI3L1+TIMP3+SPARC+COL1/3/4A1+* population (C9), a *CD1C+CD1A+AREG+* dendritic cell  
104 cluster (C6) and four distinct monocytic/macrophage populations (C1, C2, C5, and C7).

105 Out of the three microglial clusters, C4 has several pro-inflammatory markers including interferon  
106 signature genes (ISGs)- *IFI27*, *IFI16*, *IFI6* (Fig. 1C). In contrast, C0  
107 (*APOE+TREM2+CD81+OLR1+HLA-DPA+C1Q+*) and C8 (*OLFML3+ P2RY13+*) are noted to  
108 express suppressive markers such as *VEGFA*, *CCL4* (C0) and *SPP1*, *CCL4*, *ARG2* (C8)  
109 respectively (Fig. 1C). Expression of immune-suppressive markers such as *MRC1*, *CD163*,  
110 *TGFBI* and *SELENOP* was also noted in brain- associated macrophage cluster (C3) (Fig. 1C).  
111 Additionally, all the monocytic macrophage clusters display a predominantly suppressive  
112 phenotype. We noted the presence of a pro-angiogenic/hypoxic  
113 *FN1+SPP1+MIF+BNIP3+HMOX1+CXCL8+ANXA2+* cluster (C2), a *KLF2+KLF6+IL10+NR4A1+*  
114 cluster (C1), a *S100A9+MARCO+CXCL1+CXCL2+CXCL8+CRIP1+ANXA2+* cluster (C5) and a  
115 *CCL4+CXCL2+CXCL8+IL10+AREG+NLRP3+* cluster (C7) (Fig.1C). Overall, this analysis  
116 highlighted the enrichment of suppressive myeloid cell subsets in GBM tumors resected from  
117 patients.

118 To identify epigenetic factors which are critical for the regulation of immune-suppressive  
119 phenotype and function in the tumor microenvironment (TME), we investigated gene expression  
120 of several canonical epigenetic modifiers previously implicated in the regulation of myeloid cell  
121 polarization and function (Fig. 1D)<sup>26,27</sup>. Interestingly, amongst the selected epigenetic enzymes,  
122 we noted high levels of expression and selective enrichment of *KDM6B/JMJD3* in the myeloid  
123 cells, specifically in the subsets expressing immune-suppressive markers such as *CSF1R*, *KLF2*,  
124 *KLF6*, *CXCL8* and *SPP1* (Extended Data Fig.1B-C). H3K27 methylation is an important  
125 epigenetic determinant of myeloid cell phenotype and function<sup>36</sup>. *KDM6B* works in tandem with  
126 other epigenetic modifiers such as *KDM6A* and *EZH2* in the regulation of H3K27 mediated gene  
127 expression. Unlike *KDM6B*, *KDM6A* and *EZH2* showed minimal expression in the intratumoral  
128 myeloid cell subsets (Fig.1D). Next, to confirm our findings, we used two independent scRNA seq  
129 datasets with n=4<sup>32</sup> and n=20<sup>37</sup> GBM patients respectively. Analyses of these two datasets  
130 demonstrated distinct *CD3E*+ T cell and *CD68*+ myeloid cell clusters (Extended Data Fig. 2A-D).  
131 Importantly, similar to our primary cohort of GBM patients, *KDM6B* enrichment was observed in  
132 intratumoral immune-suppressive myeloid cells (Extended Data Fig. 2A-D).

133 Next, we performed spatial transcriptomic analysis of GBM tumors (n=3) resected from patients  
134 (characteristics enlisted in Supplementary Table 1) using the 10X-Genomics Visium platform.  
135 Hematoxylin and Eosin (H&E) staining was done to determine the overall architecture of each  
136 tumor section (Fig S3A). Immunofluorescence microscopy demonstrated the presence of  
137 intratumoral CD3+, CD8+ T cells and CD68+CD163+ myeloid cells (inset) and confirmed that  
138 human GBM tumors are diffusely infiltrated with myeloid cells (Fig. 1E). Further,  
139 immunohistochemical (IHC) staining confirmed the expression of *KDM6B* protein in all the human  
140 GBM sections studied (Extended Data Fig.3B). To visualize the spatial localization of *KDM6B*+  
141 immune-suppressive myeloid cells in the GBM TME, we used matched scRNA seq data to embed  
142 single cells to their spatial coordinates in tissue sections by applying CellTrek<sup>38</sup>. Multiple myeloid

143 cell, T cell, B cell, and NK cell clusters could be spatially delineated based on characteristic gene  
144 signatures (Fig.1F,G, Extended Data Fig.4A-D and Extended Data Fig.5A-C). As expected, we  
145 noted inter-tumoral qualitative and quantitative heterogeneity in the spatial landscape of immune  
146 cell subsets. However, enrichment of *KDM6B* expressing myeloid clusters co-expressing  
147 immune-suppressive markers such as *SPP1*, *CXCL8*, *MARCO* and *MAFB* was observed across  
148 all the tumor sections studied (Fig. 1F-H, Extended Data Fig. 4A-F and Extended Data Fig. 5A-  
149 C).

150 Together, single-cell and spatial transcriptomic analyses of human GBM tumor samples  
151 demonstrated the expression of *KDM6B* in the immune-suppressive myeloid cell subsets in  
152 patients with GBM.

153

#### 154 **Myeloid cell-specific deletion of *Kdm6b* improves survival in preclinical models of GBM** 155 **and results in a pro-inflammatory milieu in murine GBM tumors**

156 To interrogate the impact of *KDM6B*-mediated regulation of the functional phenotype of myeloid  
157 cell subsets on anti-tumor immunity, we generated a murine model bearing myeloid cell-specific  
158 deletion of the *Kdm6b* gene (*LysM<sup>cre</sup>KDM6B<sup>fl/fl</sup>*) (Extended Data Fig. 6A,B). Mass cytometry  
159 (CyTOF) based immunophenotyping studies showed no significant differences in the relative  
160 abundance of the major immune cell subsets including myeloid cells in the immune cell repertoire  
161 of bone marrow, spleen, and lymph-node from wild type (control) and *LysM<sup>cre</sup>KDM6B<sup>fl/fl</sup>* mice  
162 (Extended Data Fig.6C), indicating that myeloid-specific deletion of *Kdm6b* does not alter the  
163 development of immune cell populations. Next, we orthotopically inoculated murine GBM cell line  
164 -GL261 into the brain of control and *LysM<sup>cre</sup>KDM6B<sup>fl/fl</sup>* mice. Magnetic Resonance Imaging (MRI)  
165 studies done on day 14 post tumor inoculation revealed a lower tumor burden in mice having  
166 myeloid-cell specific *Kdm6b* deletion as compared with control (Fig. 2A). We also observed a

167 similar reduction in tumor volumes in  $LysM^{cre}KDM6B^{fl/fl}$  mice bearing another murine GBM cell  
168 line- CT-2A (Fig. 2A). In addition, survival studies showed improvement in survival of both GL261  
169 and CT-2A GBM tumor-bearing  $LysM^{cre}KDM6B^{fl/fl}$  mice compared with control (Fig. 2B). Thus,  
170 *Kdm6b* expression in myeloid cell subsets potentially aids in maintaining the suppressive  
171 phenotype as constitutive deletion of *Kdm6b* in myeloid cells attenuated tumor growth and  
172 provided a survival advantage in two pre-clinical models of GBM tumor bearing mice.

173 To determine the impact of myeloid cell-specific *Kdm6b* deletion on the GBM tumor immune  
174 microenvironment, we performed scRNA sequencing of the murine GBM (GL261) tumors from  
175 control and  $LysM^{cre}KDM6B^{fl/fl}$  mice. UMAP analyses of *Cd45+* immune cell subsets revealed  
176 distinct clusters of immune cell subsets including NK cells (C2, C18), CD8 T cells (C5,11,21),  
177 CD4 T cells (C8), regulatory T cells (C6, 22), *Il17+Rorc+* T cells (C20), B cells (C13), neutrophils  
178 (C24), mast cells (C25), microglial cells (C0 and C23), conventional dendritic cells  
179 (C3,4,7,9,17,19), plasmacytoid dendritic cells (C16) and multiple subsets of monocytic  
180 macrophages (C1,10,12,14,15) (Fig. 2C, Extended Data Fig. 7A). We noted an increase in the  
181 abundance of cytotoxic *Gzmb+Ifn $\gamma$ +Cd8+* T cells (C11), NK cells (C2) with a concomitant  
182 decrease in the abundance of immunosuppressive *Cd4+Foxp3+* regulatory T cells- Tregs (C6)  
183 (Extended Data Fig. 7A,B). Further, the frequency of *Il17+* T cells (C20) was lower in the TME of  
184 GBM tumors derived from  $LysM^{cre}KDM6B^{fl/fl}$  mice compared to the control mice (Extended Data  
185 Fig. 7A,B). Overall, a high cytotoxic T lymphocyte (CTL) to Treg ratio in  $LysM^{cre}KDM6B^{fl/fl}$  mice  
186 (Extended Data Fig.7C) indicated a pro-inflammatory skewing of the intratumoral milieu  
187 characterized by a heightened anti-tumor T cell response in  $LysM^{cre}KDM6B^{fl/fl}$  mice.

188 The *LysM-cre* model used in this study harbors genetic deletion of *Kdm6b* specifically in myeloid  
189 cells<sup>39,40</sup>. Hence, the changes observed in non-myeloid immune subsets including increased T  
190 cell mediated anti-tumor immunity in the  $LysM^{cre}KDM6B^{fl/fl}$  GBM (GL261) tumor-bearing mice  
191 could be secondary to the changes in *Lyz2* expressing myeloid subsets following *Kdm6b* deletion.



192 In our scRNA seq analysis, we noted *Lyz2* expression in intratumoral monocytic macrophages,  
193 neutrophils, certain clusters of DCs and microglial cells (Extended Data Fig.7D). To investigate  
194 the functional changes in these myeloid cell subsets, we studied the differentially expressed  
195 genes (DEGs) in these subsets from control and *LysM<sup>cre</sup>KDM6B<sup>fl/fl</sup>* mice. This analysis revealed  
196 that depletion of *Kdm6b* significantly altered the transcriptomic landscape of intratumoral myeloid  
197 cells in GBM tumor-bearing mice. Expression of several pro-inflammatory genes such as those  
198 involved in phagocytosis (*Fcgr3*, *Lgals3*, *Cltb*, *Arpc3*, *Arf1*), antigen presentation (*H2-Ab1*, *H2-*  
199 *Eb1*) as well as several ISGs (*Oas1a*, *Isg15*, *Irf7*, *Cxcl9* and *Cxcl10*) were upregulated whereas  
200 genes associated with immune-suppression such as *Zeb2*, *Klf2* and *Klf6* were downregulated in  
201 monocytic macrophages (Fig. 2D) and DCs (Fig. 2E). Next, we performed Gene Set Enrichment  
202 Analysis (GSEA) with the DEGs which revealed the differences in the major functional pathways  
203 in the intratumoral monocytes, macrophages and DCs derived from control and *LysM<sup>cre</sup>KDM6B<sup>fl/fl</sup>*  
204 GBM (GL261) tumor-bearing mice. Prominent enrichment of Fc Gamma Receptor mediated  
205 phagocytosis, antigen presentation pathway as well as type I and type II interferon response was  
206 observed upon *Kdm6b* deletion (Fig.2F). In addition to the transcriptomic changes, we noted a  
207 decrease in the abundance of tumor-infiltrating neutrophils and mast cells (Extended Data  
208 Fig.7A,B). Further, we observed a concomitant increase in the abundance of pDCs (C16), a major  
209 type I interferon producing cells <sup>41</sup> and migratory cDC1s (C7) which are known to be efficient  
210 antigen-presenters <sup>42,43</sup> in *LysM<sup>cre</sup>KDM6B<sup>fl/fl</sup>* mice compared to the control (Extended Data Fig.  
211 7A,B). Of note, migratory cDC1s express *Lyz2* while pDCs lack expression of *Lyz2* (Extended  
212 Data Fig. 7D). Hence, the changes in migratory DCs could be directly attributed to *Kdm6b*  
213 deletion, while the effect on pDCs could be due to changes in the TME. Cumulatively, the findings  
214 from scRNA seq demonstrated a global transcriptomic change in intratumoral myeloid cell subsets  
215 in the absence of *Kdm6b*, leading to a pro-inflammatory milieu in the GBM TME. Additionally,  
216 mass cytometry analysis (Extended Data Fig. 8A,B) of GBM tumors from CT-2A tumor bearing  
217 control and *LysM<sup>cre</sup>KDM6B<sup>fl/fl</sup>* mice showed a decrease in the abundance of PDL1+TGFβ+ (C26)

218 and CD115+TGF $\beta$ + (C15) suppressive myeloid cell clusters (Extended Data Fig. 8B,C) in the  
219 absence of *Kdm6b* with a concurrent increase in the abundance of GZMB+ CD8 T cells (C22)  
220 (Extended Data Fig. 8B,C) and the CTL to Treg ratio (Extended Data Fig. 8D). Thus scRNA seq  
221 and CyTOF analysis of tumors derived from two pre-clinical GBM models demonstrated that the  
222 absence of *Kdm6b* in myeloid cells results in a pro-inflammatory milieu in murine GBM tumors.

223

### 224 ***Kdm6b* deletion alters the abundance and transcriptomic landscape of intratumoral** 225 **monocytes and macrophages**

226 To gain a deeper understanding of the transcriptomic changes in the highly abundant  
227 monocytes/macrophages in the GBM TME following *Kdm6b* deletion, we performed reclustering  
228 of *Itgam*+ clusters C0,1,10,12,14,15,23 (Fig. 3A, Extended Data Fig. 9A). Annotation of all the  
229 distinct cell subsets demonstrated several monocytic macrophage clusters (C1-9, 11), brain-  
230 associated macrophages (C0) as well as a microglial cluster (C10) in the GBM TME (Fig. 3A,  
231 Extended Data Fig. 9A,B). Overall, we noted a decrease in the infiltration of *Chil3+Ccr2+S100a4+*  
232 classical monocytic macrophages (C7) in the LysM<sup>cre</sup>KDM6B<sup>fl/fl</sup> tumor-bearing mice (Fig. 3B,C).  
233 Clusters expressing antigen presenting molecules (*H2-Eb1+H2-Ab1+H2-Aa+Ciita+*)(C2),  
234 interferon signature genes (*Isg15>Ifit+Irf7+Rsad2+Isg20+Tlr2+Cxcl9+Cxcl10+*)(C3) and  
235 phagocytic genes (*Lgals3+Gpnmb+Fabp5+*)(C9) were more abundant in LysM<sup>cre</sup>KDM6B<sup>fl/fl</sup> GBM  
236 tumor-bearing mice whereas cluster expressing immunosuppressive genes  
237 (*Klf2+Klf4+Zeb2+Atf4+Mafk+Klf6+*)(C6) were more abundant in GBM tumors derived from control  
238 mice (Fig. 3B,C). In addition to cellular abundance, comparison of gene expression patterns of  
239 these five individual clusters between GBM tumors derived from control and LysM<sup>cre</sup>KDM6B<sup>fl/fl</sup>  
240 mice showed an increase in the expression of several MHC molecules in C2 indicating  
241 enhancement of their ability to present antigens as well as increased *Myd88*, *Irf5*, *Isg20*, *Ifitm3*,  
242 *Oas1a*, *Isg15* in C3, indicating stronger interferon signaling in response to *Kdm6b* deletion (Fig.

243 3C). Further, immune-suppressive clusters C6 and C7 also showed significant upregulation of  
244 pro-inflammatory genes following *Kdm6b* deletion (Fig. 3C).

245 Together, these findings revealed that the absence of *Kdm6b* in monocytes/macrophages leads  
246 to upregulation of pro-inflammatory gene expression, thus regulating the phenotypic plasticity of  
247 intratumoral myeloid cells.

248

249 **Myeloid cell-specific deletion of *Kdm6b* alters the chromatin landscape of key genes**  
250 **regulating the functional phenotype of intratumoral myeloid cells**

251 To determine the chromatin landscape responsible for the changes in the gene expression  
252 observed in response to *Kdm6b* deletion, we performed scATAC seq of CD45+ cells sorted from  
253 the GBM (GL261) tumors of control (n=5, pooled) and *LysM<sup>cre</sup>KDM6B<sup>fl/fl</sup>* mice (n=5, pooled).  
254 Single-cell ATAC profiling of the immune cell compartment of GL261 tumors followed by UMAP  
255 analysis showed distinct immune cell subsets (Fig. 4A,B, Fig. S10A). Genes proximal to cluster-  
256 specific cis-elements were also used to annotate individual cell types (Fig. 4C). Briefly, C(0-2,6)  
257 showed accessibility at cis-elements neighboring macrophage associated genes, including *Mafb*,  
258 *Cebpb* and *F10*; C(10,13) demonstrated accessible cis-elements proximal to DC associated  
259 genes such as *Mreg*, *Nr4a3* and *Anxa3*, while C(5,14) harbored accessible cis-elements  
260 neighboring B cell associated genes, including *Fam43a*, *Cd19* and *Ms4a1* (Fig. 4C). Additionally  
261 CD4 T cells (*Cd4*, *Tcf7*, *Zap70*), CD8 T cells (*Cd8a*, *Cd8b*, *Ifng*), regulatory T cells (*FoxP3*), NK  
262 cells (*Eomes*, *Prf1*) and even rare cell subsets such as mast cells (*Homer2*, *Tbc1d8*) could be  
263 identified from accessibility profiles of cell type specific cis-regulatory elements (Fig. 4C). We also  
264 noted a prominent increase in the abundance of CTLs (C12) and a concomitant decrease in the  
265 abundance of Tregs (C21) (Extended Data Fig.10 A,B), mirroring the findings from scRNA seq  
266 and confirming the pro-inflammatory skewing of the intratumoral milieu in *LysM<sup>cre</sup>KDM6B<sup>fl/fl</sup>* mice.

267 To define the chromatin landscape of myeloid cells, we analyzed *Lyz2*<sup>+</sup> population which showed  
268 an increase in abundance of antigen presenting cluster (C0), cluster expressing IFN-related  
269 genes (C2) as well as the phagocytic cluster (C4) (Fig. 4D-F, Extended Data Fig.11A). In addition  
270 to the quantitative changes observed in the myeloid cell populations, we aimed to address the  
271 qualitative changes occurring in the different myeloid subsets in response to *Kdm6b* deletion.  
272 Interrogation of chromatin accessibility of individual genes of interest via coverage plots revealed  
273 greater accessibility of genes associated with antigen presentation such as *H2-Eb2*, *H2-Ab1* (C0),  
274 genes encoding positive regulators of phagocytosis such as *Fcgr1* and *Fcgr4* (C0) (Extended  
275 Data Fig.11B), and genes involved in interferon signaling and response such as *Ifnar1*, *Ifngr1*,  
276 *Isg15*, *Ifitm6* (C2) in *LysM<sup>cre</sup>KDM6B<sup>fl/fl</sup>* mice (Extended Data Fig.11C).

277

278 Thus, the findings from scATAC seq showed open chromatin landscape of pro-inflammatory  
279 genes in intratumoral myeloid cells in the absence of *Kdm6b*.

280

281 ***Kdm6b* regulates H3K27me3 enrichment of genes regulating phagocytosis, antigen**  
282 **presentation, and interferon response in myeloid cells**

283 As we previously mentioned, KDM6B promotes gene expression by demethylation of  
284 H3K27me3<sup>33</sup>. Therefore, to test whether the observed changes in the chromatin accessibility and  
285 gene expression leading to pro-inflammatory skewing of myeloid cells were regulated by KDM6B-  
286 mediated H3K27me3 demethylation, we performed ChIP seq assays on bone marrow derived  
287 macrophages (BMDMs) from control and *LysM<sup>cre</sup>KDM6B<sup>fl/fl</sup>* mice. ChIP using anti-KDM6B  
288 antibody allowed identification of genes directly bound by KDM6B. We identified *Socs3* and *Mafb*  
289 as direct targets of KDM6B in control BMDMs (Fig. 5A,D). Further, in BMDMs harbouring *Kdm6b*  
290 deletion there was a drastic reduction in KDM6B occupancy of these genes as expected (Fig.

291 5A,D), and a concurrent enrichment of H3K27me3 (Fig. 5B,E). We also used quantitative PCR to  
292 confirm the reduction in expression of these genes in *LysM<sup>cre</sup>KDM6B<sup>fl/fl</sup>* BMDMs (Fig. 5C,F). These  
293 findings demonstrated that KDM6B directly binds to *Socs3* and *Mafb* encoding genetic regions  
294 and demethylates H3K27me3 to induce gene expression. Hence in the absence of KDM6B, these  
295 genes are enriched for the repressive H3K27me3 marks thus inhibiting gene expression. SOCS3  
296 is a known suppressor of cytokine signalling<sup>34</sup> and MAFB has been established as a suppressor  
297 of type I IFN signalling<sup>35</sup>. Therefore, reduced expression of these immune-suppressive genes in  
298 the absence of KDM6B provides a strong rationale for the pro-inflammatory skewing of myeloid  
299 cells observed in response to *Kdm6b* deletion. Further, ChIP seq identified *Sirpa* as a direct target  
300 of KDM6B, with reduction in KDM6B occupancy (Fig. 5G) and H3K27me3 enrichment (Fig. 5H)  
301 in *Kdm6b* deleted BMDMs. SIRPA acts as a negative regulator of phagocytosis by generating  
302 “don’t-eat-me” signals<sup>19</sup>. Overall, the findings from the ChIP-sequencing study provided  
303 mechanistic insight into KDM6B mediated regulation of macrophage phenotype and function.  
304 KDM6B binds to negative regulators of interferon response and phagocytosis including *Mafb*,  
305 *Socs3* and *Sirpa*. Thus, these findings implicate KDM6B as an upstream regulator of multiple  
306 critical functional pathways in macrophages including cytokine production/response, antigen  
307 presentation and phagocytosis.

308 In order to investigate the impact of KDM6B depletion on phagocytosis and antigen-presentation  
309 functions of myeloid cells, we performed in-vitro phagocytosis and antigen-presentation assays  
310 using bone marrow derived macrophages (BMDMs) from control and *LysM<sup>cre</sup>KDM6B<sup>fl/fl</sup>* mice. We  
311 found that following stimulation with lipopolysaccharide, *Kdm6b* deficient BMDMs demonstrated  
312 enhanced phagocytosis compared to control as evident from a higher percentage of fluorescent  
313 non-coated latex bead positive BMDM cells (Fig. 5I). Additionally, phagocytosis of fluorescently  
314 labelled GL261 cells was higher by BMDMs deficient in *Kdm6b* compared to control (Fig. 5J,  
315 Extended Data Fig.11D). For antigen presentation assay we co-cultured gp100-pulsed BMDMs

316 with cell trace violet (CTV) labelled cognate T cell receptor-bearing CD8 T cells isolated from pmel  
317 mice<sup>44</sup> (Fig. 5K). Based on differences in dilution of the CTV dye, we observed that co-culture with  
318 BMDMs derived from *LysM<sup>cre</sup>KDM6B<sup>fl/fl</sup>* mice led to significantly higher T cell proliferation as  
319 compared to BMDMs derived from control mice (Fig. 5L). BMDMs pulsed with the non-cognate  
320 LCMV peptide, showed minimal proliferation thus confirming the antigen-specificity of the  
321 observed proliferation in T cells (Extended Data Fig.11E). Overall, the T cell proliferation assay  
322 indicated that *Kdm6b* deficient BMDMs are more efficient antigen presenters as compared to  
323 control BMDMs. These findings provided evidence of enhanced phagocytic and antigen  
324 presentation function of myeloid cells following *Kdm6b* deletion.

325 Cumulatively, we found that KDM6B regulates H3K27me3 enrichment of genes regulating critical  
326 pathways modulating myeloid cell functions such as phagocytosis, antigen presentation, and  
327 interferon signaling/response.

328

### 329 **Pharmacological inhibition of KDM6B improves the efficacy of immune checkpoint therapy** 330 **in GBM**

331 Since KDM6B functions upstream to several critical functional pathways, therapeutic targeting of  
332 KDM6B could revert myeloid-derived immune suppression. To determine the translational  
333 relevance of our findings from the genetic model, we compared murine GBM tumor growth and  
334 the tumor immune microenvironment in the presence and absence of a pharmacological inhibitor  
335 of KDM6B (GSK-J4)<sup>45,46</sup>. MRI studies revealed lower tumor burden in GSK-J4 treated GL261  
336 tumor bearing mice as compared with control (Fig. 6A). Additionally, we observed improvement  
337 in the overall survival of GL261 tumor-bearing mice treated with GSK-J4 (Fig. 6B). Of note, GSK-  
338 J4 which targets KDM6A/B, has been shown to inhibit proliferation of glioma cell lines in-vitro<sup>47</sup>.

339 Hence, the observed improvement in survival could be due to the direct effect of GSK-J4 on tumor  
340 cells as well as its effects on the tumor immune microenvironment.

341 Hence, to investigate the effect of GSK-J4 on the GBM tumor immune microenvironment, we  
342 performed scRNA seq. UMAP analyses performed on scRNA-seq data from GSK-J4 treated and  
343 control GL261 tumors showed distinct lymphoid (C9-12,15,17) and myeloid cell clusters (C0-  
344 8,13,14,16) (Fig. 6C,D, Extended Data Fig. 12). We noted a significant decrease in the abundance  
345 of *Cd14+Ly6c2+Plac8+Cxcl2+Vegfa*+ monocytic macrophage subset (C0) in GBM tumor-bearing  
346 mice treated with GSK-J4 (Fig. 6E). C1, characterized by the expression of markers of both  
347 activated CNS associated macrophages and disease associated microglia (*Ms4a7, Ccl8, Cd74,*  
348 *Tmem119, Hexb, Cx3cr1, Trem2, C1qa, C1qb, C1qc, H2-Ab1*) increased in abundance post  
349 treatment with GSK-J4 (Fig. 6D,E). We also identified a *Gpnmb*+ phagocytic cluster (C4) which  
350 increased in abundance in GSK-J4 treated mice (Fig. 6D,E). Importantly, we also noted an  
351 increase in the *Cd8+Gzmb+Ifng*+ cytotoxic T cells (C9) and *Cd4+Icos+Ifng+Cxcr6*+ T cell cluster  
352 (C10) in response to GSK-J4 treatment (Fig. 6D,E).

353 To corroborate the findings from the GL261 model, we used the CT-2A GBM model and treated  
354 them with GSK-J4. MRI studies revealed lower tumor burden in GSK-J4 treated CT-2A tumor  
355 bearing mice as compared with control (Extended Data Fig.13A-C). Additionally, interrogation of  
356 the TME of CT-2A GBM tumors using CyTOF (Extended Data Fig.13D,E) also showed  
357 significantly lower abundance of immune-suppressive myeloid clusters (C3,9) and higher  
358 abundance of NK cells (C12) and effector/memory CD8 T cells (C6) in GSK-J4 treated mice  
359 (Extended Data Fig.13F). Thus cumulatively, scRNA seq and CyTOF data from two distinct GBM  
360 tumor bearing murine models revealed a significant reduction in intratumoral immune-suppressive  
361 monocytic macrophage populations with a concomitant increase in effector CD8 T cell subset in  
362 response to GSK-J4 treatment.

363 Myeloid heavy tumor types such as GBM tumors often demonstrate primary resistance to immune  
364 checkpoint therapy. To test if KDM6B inhibition mediated pro-inflammatory skewing of the tumor  
365 immune microenvironment could increase the efficacy of ICT in a murine model of GBM, we  
366 treated GL261 tumor-bearing mice with vehicle, anti-PD1, GSK-J4 and the combination of anti-  
367 PD1 plus GSK-J4. We found that the combination therapy of anti-PD1 plus GSK-J4 led to a  
368 significant reduction in tumor weight (Fig. 6F) as well as in improvement in overall survival (Fig.  
369 6G). In order to understand the changes in the TME, we performed CyTOF analysis on these  
370 tumors (Fig. 6H, Extended Data Fig.14). We noted that CD8+CD86+CD44+ effector memory T  
371 cell cluster (C17) was significantly higher in mice receiving a combination of anti-PD1 plus GSK-  
372 J4 as compared with the control, GSK-J4 and anti-PD1 monotherapy groups (Fig. 6I, Extended  
373 Data Fig.14). Also, there was a significant decrease in a CD11b+F4/80+ monocytic macrophage  
374 cluster expressing CD115/CSF1R (C4) and a Ly6c+Ly6g-CD11b+F4/80+ monocytic-myeloid  
375 derived suppressor cell (M-MDSCs) cluster expressing TGF $\beta$  (C28) following treatment with the  
376 combination of anti-PD1 plus GSK-J4 (Fig. 6I, Extended Data Fig.14).

377 Together, these findings demonstrate that pharmacological inhibition of KDM6B by GSK-J4 can  
378 skew the TME of GBM tumor-bearing mice to a pro-inflammatory phenotype and reduce the  
379 frequency of several pro-tumorigenic myeloid cell subsets including M-MDSCs and *Cxcl2*+ TAMs,  
380 thus, improving overall survival and enhancing sensitivity to anti-PD1 therapy.

381

## 382 **Discussion**

383 This study identified a selective expression of KDM6B in the intra-tumoral myeloid cell subsets in  
384 the GBM tumors resected from patients utilizing single-cell transcriptomic and spatial analysis.  
385 Reverse translational studies using pre-clinical models of GBM demonstrated that targeting  
386 KDM6B-mediated epigenetic pathways in the myeloid cells via genetic deletion and



387 pharmacological inhibition resulted in upregulation of pro-inflammatory pathways, cumulatively  
388 improving survival and enhancing sensitivity to anti-PD1 therapy (Fig. 6J).

389

390 Over the years, multiple myeloid cell-specific pathways have been explored individually as  
391 potential targets for the treatment of cancer<sup>15-17</sup>. However, these pathways are highly interrelated  
392 and often redundant, therefore targeting a single pathway often fails to elicit optimum clinical  
393 benefit. We found that KDM6B is upstream of multiple pathways and inhibition of KDM6B  
394 enhanced interferon response pathways, antigen presentation, and phagocytosis in macrophages  
395 as well as in DCs. Additionally, our mechanistic studies identified certain critical regulators of the  
396 above mentioned pathways including *Mafb*, *Socs3* and *Sirpa* as direct targets of KDM6B mediated  
397 H3K27me3 demethylation. MAF BZIP Transcription Factor B (MAFB) which encodes a basic  
398 leucine zipper myeloid cell-specific transcription factor acts as a rheostat to inhibit type I IFN  
399 induction by physically blocking IRF3 from binding to its target genes<sup>35,48,49</sup>, which might provide  
400 a possible explanation for the enhanced interferon response observed upon KDM6B deletion.  
401 Further, suppressor of cytokine signaling 3 (*Socs3*) inhibits cytokine-induced JAK-STAT signaling  
402 pathways<sup>50</sup> and cytokines including IFN pathways have been shown to regulate both antigen  
403 presentation and phagocytosis by myeloid cells<sup>51-55</sup>. Additionally, KDM6B regulates *Sirpa* which  
404 acts as a negative regulator of phagocytosis by generating “don’t-eat-me” signals<sup>56</sup>. Thus,  
405 KDM6B regulates phagocytosis by modulating both activators and inhibitors of the phagocytosis  
406 pathway. Of note, the changes observed in the phagocytosis assays, though statistically  
407 significant were quantitatively modest. This might possibly be due to the in-vitro setting in which  
408 the experiments were performed, as opposed to the in-vivo intratumoral environment. Overall,  
409 our findings suggest that KDM6B functions upstream of several critical functional pathways (Fig.  
410 6J). Therefore, targeting KDM6B to reprogram the immune-suppressive myeloid population into  
411 an immune-stimulatory phenotype could potentially be an important therapeutic strategy rather  
412 than targeting individual pathways.

413 Considering the heterogeneity of the myeloid cell subsets, a single cre-flox model system can not  
414 target all the myeloid cell subsets simultaneously. We used the LysM-cre model to evaluate  
415 KDM6B-mediated epigenetic regulation of myeloid cells since *Lyz2* expression is generally  
416 observed in monocytes and macrophages, granulocytes and in some dendritic cells<sup>57</sup>. Although  
417 we noted an increase in the microglial-like cells expressing antigen presentation molecules  
418 following deletion of KDM6B, LysM-cre model is not adequate for a comprehensive interrogation  
419 of microglial cells.

420

421 Overall, based on the single-cell and spatial transcriptomic analysis of human GBM samples and  
422 the series of reverse translational studies using multiple pre-clinical model systems, we identified  
423 a KDM6B-mediated immunoregulatory program in myeloid cells, providing a strong rationale to  
424 consider evaluating KDM6B inhibition as a therapeutic strategy to overcome myeloid-derived  
425 immune suppression and enhance response to immune-based therapies. The strategy of  
426 inhibiting KDM6B, proposed in this study, not only adds to the existing repertoire of myeloid cell  
427 targeting strategies, it proposes a new paradigm of regulating the epigenetic machinery to target  
428 intratumoral myeloid cell plasticity thus reprogramming them to a pro-inflammatory phenotype.

429

#### 430 **Methods:**

431 **Patients.** Patient samples were collected after appropriate informed consent was obtained on MD  
432 Anderson internal review board (IRB)-approved protocol PA13-0291. All patients signed informed  
433 consents for participation in PA13-0291 before surgery or sample collection. The clinical  
434 characteristics of individual patients are shown in Supplementary Table 1.

435 **H&E and IHC staining.** Hematoxylin and Eosin (H&E) and IHC staining were performed on  
436 formalin-fixed, paraffin-embedded tissue sections. Tissues were fixed in 10% formalin, embedded

437 in paraffin, and sectioned at four-micron–thickness. For IHC, sections were antigen retrieved with  
438 ER solution 1 (Leica Microsystems, catalog no. AR9961), protein block was applied for 30 mins  
439 (Leica Microsystems, catalog no. RE7102) and stained with KDM6B (ThermoFisher, catalog no.  
440 PA5-32192) at 1:200 dilution followed by rabbit anti-human secondary. 3'-3-diaminobenzidine  
441 (DAB) substrate (Leica Microsystems) was used as a chromogen followed by hematoxylin  
442 counterstain. Slides were scanned and digitalized using the scanscope system from Scanscope  
443 XT, Aperio/Leica Technologies. IHC staining was interpreted in conjunction with H&E stained  
444 sections.

445 **Immunofluorescence.** Using the Opal multiplex immunofluorescence staining protocol<sup>54</sup> on a RX-  
446 BOND (Leica) autostainer, GBM tissue sections were stained for CD3 (Dako, A0452, 1:200  
447 dilution), CD8 (LS-Bio, C8/144b, 1:100 dilution), CD68 (Dako, PGM-1, 1:25 dilution) and CD163  
448 (Leica Microsystems, 10D6, 1:20 dilution). Subsequent visualization was performed using Akoya  
449 Opal fluorophores (620, 520, 480, 570 respectively), DAPI (1:2000 dilution) and cover-slipped  
450 using Vectashield Hardset895 mounting medium. Slides were scanned using a Vectra/Polaris  
451 slide scanner (PerkinElmer) and images acquired at 20X magnification were spectrally unmixed  
452 using Inform software (Akoya).

453 **Spatial Transcriptomics Assay (10X Genomics, Visium).** GBM tumors were paraffin  
454 embedded and serially sectioned (thickness 5  $\mu$ m). Formalin-fixed paraffin-embedded (FFPE)  
455 tissue from 3 GBM samples were used for spatial transcriptomics analysis. FFPE samples were  
456 tested for RNA quality with an DV200 > 30% (Agilent). The samples were then processed  
457 according to the standard Visium Spatial Gene Expression protocol (10x Genomics) using the  
458 Visium Spatial Gene Expression Slide & Reagent Kit (10x Genomics).

459 Libraries were cleaned up using SPRI select reagent and quantified using the High Sensitivity  
460 DNA Kit run on Agilent 2100 Bioanalyzer and also KAPA Illumina library quantification kit (Roche,

461 7960140001) run on LightCycler 480. Library pool was quantified on Bioanalyzer and with  
462 quantitative PCR and sequenced using Illumina NextSeq 500.

463 **Visium spatial transcriptomics data analysis using Spaceranger and CellTrek.** The raw  
464 spatial sequencing data was processed in the Spaceranger workflow (10X Genomics). The  
465 spaceranger (version 2.0.0) mkfastq pipeline was used to convert Illumina sequencer's binary  
466 base call (BCL) files into FASTQ format. Samples were then run through the spaceranger count  
467 pipeline, which performs alignment, tissue detection, fiducial detection, and barcode/unique  
468 molecular identifier counting. Human GBM scRNA seq data analyses were performed using  
469 standard Seurat data analysis pipeline including log normalization, scaling, variable genes  
470 selection (n=3,000) using vst, dimension reduction using principal component analysis (PCA) and  
471 UMAP. Spatial transcriptomics (ST) data (10x Genomics Visium) was analyzed similar to the  
472 scRNA seq data with Seurat data analysis package (log normalization, scaling, variable genes  
473 identification and dimensionality reduction). To analyze ST data using CellTrek<sup>38</sup>, we first ran traint  
474 to coembed the data into a shared feature space with default parameters. Then we ran Celltrek  
475 on the coembedded traint data with following parameters: intp\_pnt =5,000 spots, nPCs =30, ntree  
476 =1,000, top\_spot =5, spot\_n =5 and repel\_r =3 with ten iterations. To visualize the ST data, we  
477 used celltrek\_vis tool which allows mapping any continuous or categorical cell features to the  
478 spatial map with different colors.

479 **Mice.** 5–7-weeks old C57BL/6 mice were purchased from the National Cancer Institute (NCI). 5–  
480 7-weeks old KDM6b<sup>fl/fl</sup>(B6.Cg-Kdm6b<sup>tm1.1Rbo</sup>/J, Stock no. 029615) mice and LysM<sup>cre</sup> (B6.129P2-  
481 Lys2<sup>tm1(cre)lfo</sup>/J, Stock no. 004781) mice were purchased from the Jackson Laboratory. Female  
482 mice were used for the experiments. All mice were kept in specific pathogen-free conditions at  
483 the Animal Resource Center, University of Texas MD Anderson Cancer Center. Animal protocols  
484 were approved by the Institutional Animal Care and Use Committee of the University of Texas  
485 MD Anderson Cancer Center.

486 LysM<sup>cre</sup>Kdm6b<sup>fl/fl</sup> mice were generated by breeding KDM6b<sup>fl/fl</sup> and LysM<sup>cre</sup> mice<sup>39,40</sup>. PCR based  
487 genotyping study was done to confirm *Kdm6b* deficiency using primers with the following  
488 sequences

Forward- 5'-CAG CGA TCC TGA CTT GTT CA-3'

Reverse- 5'-GTG CCA AGG CTG GAG GA-3'

489 **Mass cytometry based immunophenotyping assay.** Spleen, bone marrow and lymph node  
490 were collected from control and LysM<sup>cre</sup>Kdm6b<sup>fl/fl</sup> mice. Single-cell suspensions were generated  
491 by physical dissociation and passage through 70µm filters. Cells were washed in RPMI media by  
492 centrifugation at 2,000 rpm, 4 °C for 5 minutes. Upto 3× 10<sup>6</sup> cells were washed with FACS buffer  
493 containing 5% FBS (Fetal Bovine Serum) in PBS (Phosphate Buffered Saline) and then incubated  
494 with blocking buffer containing a mixture of 2% of bovine, murine, rat, hamster, rabbit serum and  
495 25 µg/mL 2.4G2 antibody (Fc block) in PBS at 4 °C for 10 min. Next, surface staining was done  
496 with antibody mixture (Supplementary Table 2) at 4 °C for 30 min. Following incubation, 194Pt  
497 monoisotopic cisplatin (Fluidigm) in PBS at a final concentration of 5 µM, was incubated with the  
498 samples for 3 min. Next, samples were washed twice with FACS buffer followed by fixation and  
499 permeabilization for 1 hour at 4°C. After a wash with permeabilization buffer (Invitrogen)  
500 intracellular staining was done for 30 mins at 4°C (Supplementary Table 2). Following staining,  
501 samples were washed twice with Maxpar barcode perm buffer (Fluidigm) and labeled using  
502 palladium barcoding as per the manufacturer's protocol for 30 min at room temperature. Following  
503 2 washes with FACS buffer, samples were fixed using 1.6% paraformaldehyde in PBS  
504 supplemented with 100 nM iridium nucleic acid intercalator (Fluidigm) and left overnight. Next  
505 day, cells were washed twice with PBS, filtered, and resuspended in nuclease free water.  
506 Barcoded samples were then acquired in a Helios mass cytometer (Fluidigm).

507 **Cell lines and tumor models.** The murine GBM cancer cell line GL261 was obtained from NCI  
508 and the CT-2A cell line was obtained from Millipore Sigma. GL261 and CT-2A cells were cultured

509 in complete (supplemented with 10% FBS) DMEM media at 37 °C and 5% CO<sub>2</sub>. Cells in the  
510 logarithmic phase of growth were harvested by trypsinization and washed twice with PBS before  
511 intracranial inoculation. 5X10<sup>4</sup> GL261 cells were resuspended in 3µl of 70% PBS and 30%  
512 Matrigel while 5X10<sup>4</sup> CT-2A cells were resuspended in 3µl of DMEM media (without FBS) for  
513 injection with a stereotactic apparatus (Stoelting) in the cranial window- 2mm posterior and 2mm  
514 lateral to the bregma and 3mm deep into the mouse cerebrum.

515 **MRI image quantification.** The MRI images were quantified using ImageJ (NIH) v.1.52a. First,  
516 images were imported, and their brightness/contrast was adjusted. Image slices were then  
517 scanned to identify tumor sections. A gate was drawn around the tumor in each section and the  
518 area was measured. Image geometry indicated the slice thickness to be 0.75 mm and the distance  
519 between two sections to be 1 mm. The tumor area in each section was multiplied by 0.75 and the  
520 average between the tumor area in two sections was taken and multiplied by 0.25 (1 – 0.75; this  
521 gave the value for depth). The volume for each tumor was obtained by multiplying the tumor area  
522 and depth from the section-containing tumor. All values were added to determine tumor volume  
523 in mm<sup>3</sup>.

524 **Tumor harvesting and processing.** GL261 tumors were harvested on day 17 post tumor  
525 inoculation and CT-2A tumors were dissected on day 22 post tumor inoculation. Following  
526 dissection, tumor samples were enzymatically digested with 0.66mg/ml Liberase TL (Roche) and  
527 20mg/ml DNase I (Roche) in RPMI cell culture media for 30 minutes at 37 °C. Single-cell  
528 suspensions were generated by passing digested tumors through 70-µ filters and washed in  
529 complete RPMI media by centrifugation at 2,000 rpm 4°C for 5 minutes. Percoll gradient  
530 centrifugation at 512g for 20 minutes at 18°C was used to deplete the myelin layer and the single  
531 cell suspension obtained was counted in an automated cell counter for downstream analysis.

532 **Single cell RNA sequencing.** Single cell suspension of human and murine GL261 GBM tumors  
533 were made using the protocol described above. Single cells were incubated with a surface

534 staining cocktail of fluorescently conjugated antibodies, which included CD45 Pacific Blue (clone  
535 30-F11, Biolegend, 103126), and live/dead discrimination viability dye Pacific Orange (Invitrogen,  
536 L34968). CD45+ cells were sorted directly into 5% FBS using a FACS AriaFusion cell sorter (BD).  
537 Cells from each sample were counted before 16,000 cells per sample were loaded on the 10x  
538 chromium chip (Chromium platform, 10x Genomics), with a target of 10,000 cells per sample for  
539 the downstream analysis. Single-cell mRNA libraries were built using the Chromium Next GEM  
540 Single Cell 3' Library Construction V3 Kit, libraries sequenced on NovaSeq 6000 using 100cycle  
541 kit, flow cell type – S2-100, run format- 28/91 and 8 i7 index.

542 **Single cell RNA sequencing data analysis.** Cellranger v3.0.2 software (10x Genomics) was  
543 used to process the sequencing reads. The “cellranger count” pipeline was used to align the reads  
544 to the mouse mm10 genome and compute the count matrix. The Seurat R package was used to  
545 perform the analysis including filtering out low-quality cells, normalizing the data, and clustering  
546 the cells. Genes presented in less than 3 cells and cells with less than 200 genes or more than  
547 6000 genes, or with more than 10% mitochondrial gene counts were excluded from downstream  
548 analysis. Potential doublets were removed with the DoubleFinder R package <sup>58</sup>. Then, the  
549 “SCTransform” function was used to normalize and log transform the raw gene counts. Anchors  
550 identified by the “FindIntegrationAnchors” function were used to integrate the datasets. Principal  
551 component analysis (PCA) was applied to the top 3000 highly variable genes and the first 30  
552 components were used for constructing a KNN graph, clustering and UMAP projection.

553 **Single cell ATAC sequencing.** GL261 tumors were dissociated from control, LysM<sup>cre</sup>Kdm6b<sup>fl/fl</sup>  
554 mice and single cell suspension of cells were made using the protocol described above. Single  
555 cells were incubated with a surface staining cocktail of fluorescently conjugated antibodies, which  
556 included CD45 Pacific Blue (clone 30-F11, Biolegend, 103126), CD3ε FITC (clone 17A2,  
557 eBioscience, 11-0032-82), CD11b APC (clone M1/70, Biolegend, 101212) and live/dead  
558 discrimination viability dye Pacific Orange (Invitrogen, L34968). CD45+ cells were sorted directly

559 into 5% FBS using a FACS AriaFusion cell sorter (BD). Cell nuclei were isolated from the sorted  
560 CD45+ cells using Nuclei Isolation for Single Cell ATAC Sequencing Protocol (CG000169 Rev  
561 D). 16,000 nuclei per sample were loaded on the 10x chromium chip (Chromium platform, 10x  
562 Genomics), with a target of 10,000 nuclei per sample for the downstream analysis. Single cell  
563 ATAC libraries were built according to the manufacturer's protocol (Chromium Next GEM Single  
564 Cell ATAC Reagent Kits (v1) User Guide - CG000168 Rev D). The libraries were pooled and  
565 sequenced using NovaSeq6000 instrument with Read1 (50 cycles), Read2 (49 cycles), Index1 (8  
566 cycles), and Index2 (16 cycles). The sequencing reads were demultiplexed based on sample  
567 index barcodes.

568 **Single cell ATAC sequencing data analysis.** Cellranger-atac v1.2 software (10x Genomics)  
569 was used to process the sequencing reads. The "cellranger-atac count" pipeline was used to align  
570 the reads to the mouse mm10 genome and to perform peak calling with the default parameters.  
571 In case the detected cell number from the auto cell detecting algorithm was unexpected, the "force-  
572 cells" parameter for the "cellranger-atac count" was manually set according to the Barcode Rank  
573 Plot in the web summary result. Peak barcode count matrices from all the samples were  
574 aggregated using the "cellranger-atac aggr" pipeline function and normalized to sequencing  
575 depth. The single-cell ATAC data analysis mainly was done using the Signac (version 1.1.0)  
576 (<https://github.com/timoast/signac>) and Seurat<sup>59</sup>(version 3.2.0) R packages.

577 Cluster-wise peak calling was performed with MACS2 as previously described<sup>60</sup>. Briefly, the  
578 mouse genome was tiled into 2.5 kb size windows and a cell-by-window sparse matrix was  
579 computed by the Signac "FeatureMatrix" function. The matrix was binarized and the top 20000  
580 most accessible sites across all cells were used to cluster the cells. Peak calling for each cluster  
581 was performed by the Signac "CallPeaks" function and a union peak set of 180413 was created.  
582 Then, a cell-by-peak sparse count matrix was computed by the Signac "FeatureMatrix" function  
583 and used for downstream analysis.



584 Peaks presented in less than 10 cells and cells with less than 200 peaks were removed from the  
585 downstream analysis. Quality control matrixes including percentage reads in peaks, blacklist ratio,  
586 nucleosome signal and TSS enrichment score were calculated following the Signac vignettes.  
587 Cells with peak region fragment count between 3000 ~ 50000, percentage reads in peaks > 50,  
588 blacklist ratio < 0.025, nucleosome signal < 4, and TSS enrichment score > 2 were considered  
589 for further analysis (total 17380 cells).

590 The peak barcode count matrix was binarized and was normalized by term frequency-inverse  
591 document frequency (TF-IDF) using the Signac “RunTFIDF” function. Dimensional reduction was  
592 performed with a singular value decomposition (SVD) on the TD-IDF normalized matrix using the  
593 Signac “RunSVD” function including all the peaks. Since the first LSI component usually captures  
594 the sequencing depth variation, it was removed for the downstream analysis. Graph-based  
595 clustering, and non-linear dimension reduction for visualization were performed using the Seurat  
596 “RunUMAP”, “FindNeighbors”, and “FindClusters” functions with the 2 to 50 LSI components and  
597 resolution of 1.4. To find differentially accessible perks between two groups of cells, the Seurat  
598 “FindMarkers” function was used to with the parameter “test.use = “LR”, latent.vars =  
599 “peak\_region\_fragments”. The identified peaks was annotated on the basis of its nearest gene  
600 using the Signac “ClosestFeature”. Peak visualization was performed with the Signac  
601 “CoveragePlot” function.

602 Gene activity score was calculated using the Cicero (version 1.3.4) and Monocle3 (version 0.2.2)  
603 R package as described previously<sup>61</sup>. The binary filtered peak counts matrix from the Seurat  
604 object was used to build a Monocle3 Cell Data Set (cds) object. A Cicero cds object was created  
605 using the Cicero “make\_cicero\_cds” function with the parameter reduced\_coordinates equal to  
606 the UMAP coordination in the Seurat object. Co-accessibility scores between peaks were  
607 calculated using the Cicero “run\_cicero” function with the mouse mm10 genome. The gene  
608 activity score was calculated using the Cicero “build\_gene\_activity\_matrix” function and

609 normalized with the Cicero “normalize\_gene\_activities” function. The gene activity score was  
610 transformed with  $\log(\text{score} * 1000000 + 1)$ . The unnormalized and normalized gene activity matrix  
611 were used to create a “RNA” assay in the Seurat object for downstream analysis. To find  
612 differentially gene activity between two groups of cells, the Seurat “FindMarkers” function was  
613 used.

614 **BMDM generation.** Dissected femurs from 6-8 weeks old control and  $\text{LysM}^{\text{cre}}\text{KDM6B}^{\text{fl/fl}}$  mice  
615 were collected in ice cold complete RPMI 1640 media. Both epiphyses were removed before the  
616 bones were placed in sterile microfuge tubes and centrifuged at 500g for 5 minutes at 4 °C to  
617 extrude the bone marrow. The collected bone marrow was homogenized by pipetting followed by  
618 RBC lysis. The single cell suspension of bone marrow cells obtained, was counted in an  
619 automated Vicell cell counter before  $2 \times 10^6$  cells/well were cultured in Iscove’s Modified  
620 Dulbecco’s Medium (IMDM) supplemented with 10% FBS and 10ng/ml Macrophage colony-  
621 stimulating factor (M-CSF) (Biolegend), (growth media) in a 12 well plate. On Day 3, cells were  
622 resuspended in fresh growth media and on Day 7, cells were passaged in fresh complete IMDM  
623 containing 100ng/ml LPS (InvivoGen). On Day 8, the generated BMDMs were subjected to  
624 antigen presentation and phagocytosis assay as outlined below.

625 **ChIP sequencing.** Both LPS stimulated and unstimulated BMDMs generated as described  
626 above, were subjected to ChIP using the MAGnify Chromatin Immunoprecipitation System  
627 (Applied Biosystems) according to the Manufacturer’s protocol. Briefly, following crosslinking with  
628 formaldehyde for 10 minutes, cells were resuspended in lysis buffer and subjected to sonication  
629 to shear the DNA to 150-300 kb fragments. For each immunoprecipitation reaction 10 $\mu$ g of anti-  
630 KDM6B (Active Motif) and anti H3K27me3 antibodies (Active Motif) were used. Following antibody  
631 incubation, samples were washed and the DNA was purified and eluted. DNA concentration was  
632 measured in Qubit using the dsDNA HS Assay kit (Invitrogen) and 10 $\mu$ g of DNA was sent for

633 sequencing to the MD Anderson Cancer Center Advanced Technology Genomics Core where  
634 sequencing was done using the NextSeq500 instrument.

635 **ChIP sequencing data analysis.** The quality of CHIPseq FASTQ sequences generated as  
636 described above, were assessed using FastQC, followed by mapping by bowtie2<sup>62</sup> with mouse  
637 reference genome mm10. The bam files obtained from mapping were further processed using  
638 SAMBLASTER<sup>63</sup> and SAMTOOLS<sup>64</sup>, for duplicate removal, sorting and indexing. SAMBAMBA<sup>65</sup>  
639 was used to Normalize bam files per read counts by performing random sampling. The ChIP-seq  
640 signal enrichment over "Input" background was identified using Model based analysis of ChIP-  
641 seq (MACS) version 3<sup>66</sup>.The identified peaks were annotated using CHIPseeker<sup>67</sup>,  
642 clusterProfiler<sup>68</sup> and AnnotationDbi. Quantitative comparisons of different datasets were  
643 performed with MAnorm<sup>69</sup>. The profile plots for specific genes were plotted using computeMatrix  
644 and plotProfile programs of deepTools<sup>70</sup> and the gene tracks were plotted using EASEq version  
645 1.111<sup>71</sup>.

646 **RNA isolation and real-time PCR.** Total RNA was isolated from LPS stimulated BMDMs  
647 generated from control and LysM<sup>cre</sup>KDM6B<sup>fl/fl</sup> mice using the TriZol (Invitrogen) method according  
648 to the Manufacturer's protocol. 1µg of the RNA was reverse transcribed into complementary DNA  
649 (Superscript III cDNA kit from Invitrogen, USA) and the cDNA was used to measure the  
650 expression of genes of interest via Real Time PCR (Applied Biosystems 7500 Fast, USA). Primers  
651 used for real time PCR are as follows-

MuSocs3 Forward- 5'-CGCCCAGGTCCTTTGCCTGA-3'

MuSocs3 Reverse- 5'-CCGCATCCCGGGGAGCTAGT-3'

MuMafb Forward- 5'-GGCAGGGAGTCTCTGTCTGGC-3'

MuMafb Reverse- 5'-CAGGCCCTCCGACCCCATCT-3'

652 **Phagocytosis assay with beads.** Uncoated carboxylate modified polystyrene fluorescent  
653 orange beads (Sigma Aldrich) were added to 1X10<sup>5</sup> BMDMs generated using the protocol outlined

654 above, at a ratio of 500:1. The cells were incubated at 37 °C and 5% CO<sub>2</sub> for 4 hours before being  
655 washed in PBS, fixed in 1% PFA and acquired in a flow cytometer to monitor uptake of beads by  
656 the cells.

657 **Phagocytosis assay with GL261 cells.** CellTrace Far Red (Invitrogen) labelled GL261 cells  
658 were mixed with CTV labelled BMDMs (generated as described above) at at ratio of 1:1 and  
659 incubated at 37°C and 5% CO<sub>2</sub> for 2 hours before the mixture was washed with PBS, fixed in 1%  
660 PFA and acquired in a flow cytometer to measure the uptake of GL261 cells by the BMDMs.

661 **Antigen presentation assay.** BMDMs generated above were pulsed with GP100 (1µg/ml) or  
662 LCMV (1µg/ml, negative control) peptides (AnaSpec). Additionally, naïve CD8 T cells were  
663 isolated from the spleen of pmel mice (having CD8 T cells bearing T cell receptors specific for the  
664 gp100 antigen) by magnet-assisted cell sorting (Naïve CD8+ T cell isolation kit, Miltenyi Biotec)  
665 and stained with Cell Trace Violet (CTV, Invitrogen). Subsequently, the antigen pulsed  
666 macrophages and stained naïve CD8 T cells were co-cultured at a ratio of 1:2 for 3 days, washed,  
667 fixed and subjected to flow cytometry (BD LSR II) to measure CTV dilution as a measure of T cell  
668 proliferation in response to antigen presentation by the different BMDMs. FlowJo software v10  
669 was used for analysis.

670 **GSK-J4 and anti-PD-1 treatment regimen:** 5–7-weeks old C57BL/6 mice bearing GL261 or  
671 CT-2A tumors were treated with KDM6B inhibitor (GSK-J4; Sigma-Aldrich); 1mg per mouse, in  
672 200ul volume (3% DMSO+ 97% sterile water - vehicle) via oral gavage daily starting from day 3  
673 post tumor inoculation to the end of the experiment. GL261 tumor bearing mice were also injected  
674 intraperitoneally with 200µg, 100µg and 100µg of α-PD1 (RMP1-14; Bio X Cell) on day 7, 10 and  
675 13 respectively and sacrificed on day 17 for downstream analysis.

676 **Mass cytometry to study TME.** GL261 and CT-2A tumor tissues were dissected, processed,  
677 stained with antibodies and acquired in a mass cytometer as previously described. Surface and  
678 intracellular antibodies used for this mass cytometry are mentioned in Supplementary Table 2.

679 **Mass cytometry analysis.** Files were manually gated in FlowJo v10 by using iridium for cells,  
680 event length for singlets, cisplatin for live/dead discrimination and using CD45 lineage marker for  
681 immune cells. Clustering analysis was performed using the FlowSOM and ConsensusClusterPlus  
682 packages as previously described <sup>72</sup>

683 **Statistical analyses.** R v4.0.2 and GraphPad Prism software v9 was used for the statistical  
684 analyses. The individual tests performed have been indicated in the figure legends. All in-vivo  
685 experiments had two to three independent replicates.

686

687 **Data availability.** Raw reads for the single cell RNA sequencing, single cell ATAC sequencing  
688 and CHIP-sequencing will be deposited in European Genome-phenome Archive (EGA) which will  
689 be available upon acceptance of the manuscript.

690 **Code availability.** The scRNA seq, scATAC seq and CHIP seq analyses presented in the  
691 manuscript has been performed with open source algorithms as described in the method section.  
692 Further details will be made available by authors upon request.

693

694 **Figure legend:**

695 **Fig. 1:** *Single-cell and spatial transcriptomic analyses of human GBM tumors demonstrated*  
696 *selective expression of KDM6B in immune-suppressive myeloid cells. (A)* UMAP plot of scRNA  
697 seq data depicting the different immune cell subsets (*CD45+* cells) in the TME of patients with  
698 GBM (n=5). **(B)** UMAP plot of myeloid cells obtained by reclustering the *CD68+* clusters from Fig.  
699 1A. **(C)** Dotplot showing the average expression of indicated genes as well as the percentage of  
700 cells expressing the gene in the indicated myeloid clusters shown in Fig. 1C. **(D)** Feature plots of  
701 scRNA seq data demonstrating the expression of indicated genes encoding epigenetic enzymes,  
702 in intratumoral myeloid cell clusters. **(E)** Multiplex immunofluorescence staining shows distribution  
703 of CD3 (red), CD8 (cyan), CD68 (yellow) and CD163 (magenta) in a GBM case. Inset shows  
704 CD3+, CD8+ and CD68+CD163+ myeloid cells. **(F)** UMAP plot of scRNA seq data from patient 6  
705 (Supplementary Table 1), showing *CD45+* immune cell subsets in the GBM TME used to embed  
706 single cells to their spatial coordinates in tissue sections by applying CellTrek. **(G)** Gene  
707 expression data from all the different immune cell clusters from the matched patient plotted on  
708 spatial coordinates. **(H)** Gene expression data from the *KDM6B* expressing myeloid cell clusters  
709 (black) and CD8 T cell clusters (yellow), plotted on spatial coordinates.

710 **Fig. 2:** *Myeloid cell-specific deletion of Kdm6b improves survival in preclinical models of GBM*  
711 *and results in a pro-inflammatory milieu in murine GBM tumors. (A)* Representative axial MRI  
712 images taken on day 14 post tumor inoculation, of GL261 (top panel) and CT-2A (bottom panel)  
713 tumors in control (left panel) and *LysM<sup>cre</sup>KDM6B<sup>fl/fl</sup>* mice (right panel). Box and whisker plot  
714 demonstrating the difference in tumor volume as calculated from MRI images of GL261 (top  
715 panel) (n=5/group) and CT-2A (bottom panel) (n=10/group) GBM tumors from control and  
716 *LysM<sup>cre</sup>KDM6B<sup>fl/fl</sup>* mice. Two-tailed Student's t-test was performed (\* p<0.05, \*\* p<0.01). **(B)**  
717 Kaplan Meier plot depicting the difference in survival of GL261 (top panel) and CT-2A (bottom  
718 panel) tumor-bearing control and *LysM<sup>cre</sup>KDM6B<sup>fl/fl</sup>* mice (n=10/group). Log-rank test was

719 performed (\*\*p<0.001, \*\*\*\* p<0.0001). Data is representative of 3 independent experiments. **(C)**  
720 UMAP plot of scRNA seq data showing the different immune cell subsets (*Cd45+* cells) in the  
721 GBM (GL261) TME of control and *LysM<sup>cre</sup>KDM6B<sup>fl/fl</sup>* mice (pooled 4-5 samples/group). The data  
722 is representative of 2 independent scRNA seq experiments. **(D)** Volcano plot representing  
723 differentially expressed genes between control and *LysM<sup>cre</sup>KDM6B<sup>fl/fl</sup>* mice in intratumoral  
724 monocytes, macrophages and microglial-like cells (C0,1,10,12,14,15,23 in Fig. 2C). **(E)** Volcano  
725 plot depicting differentially expressed genes between control and *LysM<sup>cre</sup>KDM6B<sup>fl/fl</sup>* mice in  
726 intratumoral DCs (C3,4,7,9,16,17,19 in Fig. 2C). Volcano Plots shows the fold change (log<sub>2</sub> Ratio)  
727 plotted against the Absolute Confidence (-log<sub>10</sub> adjusted p value) **(F)** Plots representing GSEA  
728 pathways in intratumoral monocytes, macrophages and DCs enriched in *LysM<sup>cre</sup>KDM6B<sup>fl/fl</sup>* mice  
729 as compared to control.

730 **Fig. 3:** *Kdm6b* deletion alters the abundance and transcriptomic landscape of intratumoral  
731 monocytes and macrophages. **(A)** The left panel shows UMAP plot of scRNA seq data depicting  
732 the different immune cell subsets (*Cd45+* cells) in the GBM (GL261) TME of control and  
733 *LysM<sup>cre</sup>KDM6B<sup>fl/fl</sup>* mice (pooled 4-5 samples/group, representative of two independent  
734 experiments). The right panel shows UMAP plot obtained by reclustering of highlighted *Itgam+*  
735 clusters from the left panel. **(B)** Dotplot showing the average expression of genes of interest as  
736 well as the percentage of cells in the cluster expressing the gene in the indicated myeloid clusters.  
737 **(C)** Bar plots representing the relative frequencies of indicated myeloid clusters in control and  
738 *LysM<sup>cre</sup>KDM6B<sup>fl/fl</sup>* mice. Volcano plots depicting differentially expressed genes in the indicated  
739 intratumoral myeloid cell clusters from control and *LysM<sup>cre</sup>KDM6B<sup>fl/fl</sup>* mice. The Volcano Plot  
740 shows the fold change (log<sub>2</sub> Ratio) plotted against the Absolute Confidence (-log<sub>10</sub> adjusted p  
741 value).

742 **Fig. 4:** *Myeloid cell-specific deletion of Kdm6b* alters the chromatin landscape of key genes  
743 *regulating the functional phenotype of intratumoral myeloid cells.* **(A)** UMAP demonstrating the

744 different *Cd45*<sup>+</sup> immune cell subsets in the GBM (GL261) TME of control and *LysM*<sup>cre</sup>*KDM6B*<sup>fl/fl</sup>  
745 mice as determined from scATAC seq (4-5 pooled samples/group). **(B)** UMAP depicting the gene  
746 activity score of the indicated genes in different immune cell subsets in the GBM TME of control  
747 and *LysM*<sup>cre</sup>*KDM6B*<sup>fl/fl</sup> mice. **(C)** Heatmap showing Z-scores of 153,638 cis-elements neighboring  
748 indicated genes in the scATAC seq clusters derived from Fig.4A. **(D)** UMAP representation of  
749 scATAC seq data depicting *Ilgam*<sup>+</sup> cell subsets in the GL261 TME of control and *LysM*<sup>cre</sup>*KDM6B*<sup>fl/fl</sup>  
750 mice (pooled 4-5 samples/group). **(E)** Dotplot demonstrating the average gene activity score of  
751 genes of interest as well as percentage of cells in the cluster expressing the gene in the indicated  
752 myeloid cell clusters. **(F)** Bar graphs representing the relative frequencies of indicated myeloid  
753 clusters from control and *LysM*<sup>cre</sup>*KDM6B*<sup>fl/fl</sup> mice.

754 **Fig. 5:** *Kdm6b* regulates H3K27me3 enrichment of genes regulating phagocytosis, antigen  
755 presentation, and interferon response in myeloid cells. **(A, D, G)** Profile plots depicting the  
756 probability scores of KDM6B binding at  $\pm 1$ kb regions from transcription start site (TSS) and  
757 transcription end site (TES) of the *Socs3*, *Mafb* and *Sirpa* gene loci in bone marrow derived  
758 macrophages (BMDMs) from control (grey) and *LysM*<sup>cre</sup>*KDM6B*<sup>fl/fl</sup> (blue) mice. **(B, E, H)** Genome  
759 browser view of H3K27me3 peaks at the *Socs3*, *Mafb* and *Sirpa* gene loci in control and  
760 *LysM*<sup>cre</sup>*KDM6B*<sup>fl/fl</sup> BMDMs. **(C, F)** Box and whisker plots showing the relative expression of  
761 indicated genes normalized to the expression of  $\beta$ -actin as determined by quantitative PCR. One-  
762 tailed Student's t-test was performed (\* $p < 0.05$ , \*\*\* $p < 0.001$ ,  $n = 3-6$ /condition). **(I, J)** Box and  
763 whisker plots representing the difference in phagocytic capacity between control and *Kdm6b*  
764 deficient BMDMs, based on percentage of cells taking up beads **(I)** or GL261 cells **(J)**. Two-tailed  
765 Student's t-test was performed (\*\* $p < 0.01$ ).  $n = 5-6$ /group, representative of 2-4 independent  
766 experiments. **(K)** Schematic representation of the antigen presentation and T cell proliferation  
767 assay performed. **(L)** Representative pseudocolor flow cytometry plots showing the percentage  
768 of proliferated CD8 T-cells (gated, CTV negative), upon co-culture with gp100 pulsed control and



769 *Kdm6b* deficient BMDMs. Box and whisker plot depicting the percentage of proliferated CD8 T-  
770 cells upon co-culture with control versus *Kdm6b* deficient macrophages. (n=4, \*\*p<0.01). Data is  
771 representative of two independent experiments.

772 **Fig. 6: Pharmacological inhibition of KDM6B improves the efficacy of immune checkpoint therapy**  
773 **in GBM. (A)** Box and whisker plot depicting the difference in the tumor volume as calculated from  
774 day 14 MRI images of GBM (GL261) tumors from control (vehicle treated) and GSK-J4 treated  
775 mice (n=10/group). Two-tailed Student's t-test was performed (\*\*\*\* p<0.0001). **(B)** Kaplan Meier  
776 plot demonstrating the difference in survival of GBM (GL261) tumor-bearing mice treated with  
777 vehicle and GSK-J4 (n=10/group). Log-rank test was performed (\*\*p<0.001). Data is  
778 representative of 3 independent experiments. **(C)** UMAP plot of scRNA seq data representing the  
779 different immune cell subsets (*Cd45+* cells) in the GBM (GL261) TME of vehicle and GSK-J4  
780 treated mice (pooled 4-5 samples/group). **(D)** Dotplot showing the average expression of genes  
781 of interest as well as percentage of cells in the cluster expressing the genes defining the indicated  
782 cell clusters. **(E)** Bar plots representing the frequencies of indicated immune cell clusters from  
783 vehicle and GSK-J4 treated mice as determined by scRNA seq. **(F)** Box and whisker plot  
784 representing the GBM (GL261) tumor weights from mice receiving the indicated treatments  
785 (n=5/group). Two-tailed Student's t-test was performed (\*\*p<0.01, \*\*\*p<0.001, \*\*\*\*p<0.0001). **(G)**  
786 Kaplan Meier plot depicting difference in survival of GBM (GL261) tumor-bearing mice treating  
787 with vehicle, anti-PD1, GSK-J4 and combination of anti-PD-1 plus GSK-J4. Log-rank test was  
788 performed (\*p<0.05, \*\*p<0.01, \*\*\*\*p<0.0001). Data is representative of 2 independent  
789 experiments. **(H)** t-SNE plot of CyTOF data demonstrating different immune cell subsets (CD45+  
790 cells) in the GBM (GL261) TME of vehicle, GSK-J4 and anti-PD1 treated mice (n=5/group). **(I)**  
791 Box and whisker plots showing the relative frequencies of indicated immune cell clusters from  
792 vehicle treated and therapeutic agent treated mice as determined by CyTOF (n=5/group). Two-  
793 tailed Student's t-test was performed (\*p<0.05, \*\*p<0.01, \*\*\*p<0.001, \*\*\*\*p<0.0001). **(J)** Graphical

794 summary of the findings presented in this study depicting the role of KDM6B in regulation of  
795 myeloid cell function and its importance as a therapeutic target in GBM. IFNGR- Interferon gamma  
796 receptor. IFNAR- Interferon alpha receptor. GBM- Glioblastoma.

797 **Extended Data figure legend:**

798 **Extended Data Fig. 1: (A)** Dotplot showing the average expression of indicated genes as well as  
799 the percentage of cells expressing the gene in the indicated *CD45+* immune cell clusters in the  
800 TME of patients with GBM (n=5) shown in Fig. 1A. **(B)** UMAP plot of scRNA seq data depicting  
801 the expression of *KDM6B* gene in the different immune cell subsets (*CD45+* cells). **(C)** Violin  
802 plots demonstrating the expression level of indicated genes in the different myeloid cell clusters  
803 from Fig. 1B.

804 **Extended Data Fig. 2: (A)** UMAP plot of scRNA seq data showing *CD45+* immune cell subsets  
805 in the GBM TME derived from patients with GBM (n=4)<sup>32</sup>. **(B)** Violin plots demonstrating the  
806 expression level of indicated genes in the different immune cell clusters. **(C)** UMAP plot of scRNA  
807 seq data depicting *CD45+* immune cell subsets in the GBM TME derived from patients with GBM  
808 (n=20)<sup>37</sup>. **(D)** Violin plots representing the expression level of indicated genes in the different  
809 immune cell clusters.

810 **Extended Data Fig. 3: (A)** Hematoxylin and Eosin stained GBM tumor sections. Each section  
811 represent one patient. Scale included in the images. **(B)** Representative figures showing  
812 immunohistochemical staining for KDM6B in GBM tissue samples from 3 patients (patient  
813 number: 6, 2 and 3, Supplemental Table 1)

814 **Extended Data Fig. 4: (A, B)** UMAP plots of matched scRNA seq data from patient 2 and patient  
815 3 (Supplementary Table 1) showing *CD45+* immune cell subsets in the GBM TME used to embed  
816 single cells to their spatial coordinates in tissue sections by applying CellTrek. **(C, D)** Gene  
817 expression data of all the different immune cell clusters from matched patients plotted on spatial

818 coordinates. **(E, F)** Gene expression data from the *Kdm6b* expressing myeloid cell clusters (black)  
819 and T cell clusters (yellow) plotted on spatial coordinates of two matched patients.

820 **Extended Data Fig.5(A-C)** Dotplots showing the average gene activity score of genes of interest  
821 as well as percentage of cells in the cluster expressing the gene in the indicated clusters **(A)**  
822 shown in Fig. 1F, and **(B,C)** shown in Fig. S4A,B.

823 **Extended Data Fig.6: (A)** Schematic representation demonstrating generation of the  
824  $LysM^{cre}KDM6B^{fl/fl}$  genetic murine model. **(B)** Representative image of an agarose gel showing  
825 bands depicting PCR amplified DNA from *Kdm6b* deleted homozygous mice (single 400bp band),  
826 *Kdm6b* deleted heterozygous mice (both 368 and 400bp bands), and control homozygous mice  
827 (single 368bp band).**(C)** t-SNE plots and box and whisker plots depicting the identity and  
828 abundance of different immune cell populations present in the indicated anatomical locations in  
829 control and  $LysM^{cre}KDM6B^{fl/fl}$  mice as determined from CyTOF analysis (n=3/group).

830 **Extended Data Fig. 7: (A)** Heatmap showing the expression of genes of interest in the different  
831 *Cd45+* immune cell clusters (shown in Fig. 2C). **(B)** Bar graphs depicting the frequencies of the  
832 different intratumoral immune cell subsets in control and  $LysM^{cre}KDM6B^{fl/fl}$  mice. **(C)** Bar graph  
833 representing the ratio of intratumoral CTLs and Tregs in control and  $LysM^{cre}KDM6B^{fl/fl}$  mice as  
834 determined from scRNA seq. **(D)** Violin plots depicting the expression level of *Lyz2* in different  
835 immune cell clusters in control and  $LysM^{cre}KDM6B^{fl/fl}$  mice. Data representative of two  
836 independent scRNA seq experiments.

837 **Extended Data Fig. 8: (A)** t-SNE plot of CyTOF data demonstrating different immune cell subsets  
838 (*CD45+* cells) in the GBM (CT-2A) TME of control and  $LysM^{cre}KDM6B^{fl/fl}$  mice (n=10/group). **(B)**  
839 Heatmap showing the expression of protein markers of interest in the indicated immune cell  
840 clusters as determined by mass cytometry. **(C)** Box and whisker plots representing the relative  
841 frequencies of indicated immune cell clusters from control and  $LysM^{cre}KDM6B^{fl/fl}$  mice as

842 determined by CyTOF (control n=10/group, LysM<sup>cre</sup>KDM6B<sup>fl/fl</sup> n=8/group). Two-tailed Student's t-  
843 test was performed (\*p<0.05, \*\*p<0.01, \*\*\*\*p<0.0001). **(D)** Bar plots depicting the ratio of  
844 intratumoral CTLs and Tregs in control and LysM<sup>cre</sup>KDM6B<sup>fl/fl</sup> mice as determined by CyTOF.

845 **Extended Data Fig. 9: (A)** Heatmap showing the expression of genes of interest in the different  
846 myeloid cell clusters (shown in Fig. 3A-right panel). **(B)** Bar plots representing the frequencies of  
847 intratumoral myeloid clusters from control and LysM<sup>cre</sup>KDM6B<sup>fl/fl</sup> mice. Data representative of two  
848 independent experiments.

849 **Extended Data Fig. 10: (A)** UMAP demonstrating the CTL and Treg clusters in the GBM (GL261)  
850 TME of control and LysM<sup>cre</sup>KDM6B<sup>fl/fl</sup> mice determined by scATAC seq (as shown in Fig. 4 A-B).  
851 Bar graphs depicting the frequencies and ratio of intratumoral CTLs and Tregs in control and  
852 LysM<sup>cre</sup>KDM6B<sup>fl/fl</sup> mice as determined from scATAC seq. **(B)** Coverage plots depicting the  
853 chromatin accessibility of the indicated genes in the CTL and Treg clusters.

854 **Extended Data Fig. 11: (A)** Heatmap showing the expression of genes of interest in the indicated  
855 myeloid cell clusters (shown in Fig. 4D). **(B, C)** Coverage plots depicting accessibility of indicated  
856 chromatin regions (peaks) in genes of interest. **(D)** Representative gating strategy on FlowJo for  
857 analysis of flow cytometry data showing GL261 phagocytosis by BMDMs (shown in Fig. 5J). **(E)**  
858 Representative pseudocolor flow cytometry plots showing the percentage of proliferated CD8 T-  
859 cells (gated, CTV negative), upon co-culture with LCMV pulsed control and *Kdm6b* deficient  
860 BMDMs.

861 **Extended Data Fig.12:** Heatmap representing the expression of genes of interest in the indicated  
862 *Cd45+* immune cell clusters as determined by scRNA seq (shown in Fig. 6C).

863 **Extended Data Fig. 13: (A)** Representative axial MRI images of CT-2A tumor from vehicle treated  
864 mice (left panel) and GSK-J4 treated mice (right panel), taken on day 14 post tumor inoculation.  
865 **(B)** Box and whisker plot showing the difference in CT-2A tumor volumes (determined from MRI)

866 between vehicle and GSK-J4 treated mice (n=10/ group). Two-tailed Student's t-test was  
867 performed (\*p<0.05). **(C)** Box and whisker plot depicting the difference in CT-2A tumor weight  
868 (harvested on day 22 post tumor inoculation) between vehicle and GSK-J4 treated mice  
869 (n=10/group). Two-tailed Student's t-test was performed (\*p<0.05). **(D)** Heatmap demonstrating  
870 the expression of protein markers of interest in the indicated CD45+ immune cell clusters in the  
871 GBM (CT-2A) TME of vehicle & GSK-J4 treated mice as determined by mass cytometry. **(E)** t-  
872 SNE plot of CyTOF data depicting different immune cell subsets (CD45+ cells) in the GBM (CT-  
873 2A) TME of vehicle and GSK-J4 treated mice (n=5/group). **(F)** Box and whisker plots representing  
874 the relative frequencies of indicated immune cell clusters from vehicle and GSK-J4 treated mice  
875 as determined by CyTOF (n=5/group). Two-tailed Student's t-test was performed (\*\*p<0.01).

876 **Extended Data Fig. 14:** Heatmap showing the expression of protein markers of interest in the  
877 indicated CD45+ immune cell clusters as determined by mass cytometry (shown in Fig. 6H).

878

879

880

881

882

883

884

885

886

887 References

888

- 889 1 Locati, M., Curtale, G. & Mantovani, A. Diversity, Mechanisms, and Significance of Macrophage  
890 Plasticity. *Annu Rev Pathol* **15**, 123-147, doi:10.1146/annurev-pathmechdis-012418-012718  
891 (2020).
- 892 2 Cheng, S. *et al.* A pan-cancer single-cell transcriptional atlas of tumor infiltrating myeloid cells. *Cell*  
893 **184**, 792-809 e723, doi:10.1016/j.cell.2021.01.010 (2021).
- 894 3 Broz, M. L. *et al.* Dissecting the tumor myeloid compartment reveals rare activating antigen-  
895 presenting cells critical for T cell immunity. *Cancer Cell* **26**, 638-652,  
896 doi:10.1016/j.ccell.2014.09.007 (2014).
- 897 4 Broz, M. L. & Krummel, M. F. The emerging understanding of myeloid cells as partners and targets  
898 in tumor rejection. *Cancer Immunol Res* **3**, 313-319, doi:10.1158/2326-6066.CIR-15-0041 (2015).
- 899 5 Mantovani, A. & Allavena, P. The interaction of anticancer therapies with tumor-associated  
900 macrophages. *J Exp Med* **212**, 435-445, doi:10.1084/jem.20150295 (2015).
- 901 6 Wang, T. *et al.* BRAF Inhibition Stimulates Melanoma-Associated Macrophages to Drive Tumor  
902 Growth. *Clin Cancer Res* **21**, 1652-1664, doi:10.1158/1078-0432.CCR-14-1554 (2015).
- 903 7 Engblom, C., Pfirschke, C. & Pittet, M. J. The role of myeloid cells in cancer therapies. *Nat Rev*  
904 *Cancer* **16**, 447-462, doi:10.1038/nrc.2016.54 (2016).
- 905 8 Neophytou, C. M. *et al.* The Role of Tumor-Associated Myeloid Cells in Modulating Cancer  
906 Therapy. *Front Oncol* **10**, 899, doi:10.3389/fonc.2020.00899 (2020).
- 907 9 Ruffell, B. & Coussens, L. M. Macrophages and therapeutic resistance in cancer. *Cancer Cell* **27**,  
908 462-472, doi:10.1016/j.ccell.2015.02.015 (2015).
- 909 10 Sharma, P., Hu-Lieskovan, S., Wargo, J. A. & Ribas, A. Primary, Adaptive, and Acquired Resistance  
910 to Cancer Immunotherapy. *Cell* **168**, 707-723, doi:10.1016/j.cell.2017.01.017 (2017).
- 911 11 Goswami, S., Anandhan, S., Raychaudhuri, D. & Sharma, P. Myeloid cell-targeted therapies for  
912 solid tumours. *Nat Rev Immunol*, doi:10.1038/s41577-022-00737-w (2022).
- 913 12 Cassetta, L. & Pollard, J. W. Targeting macrophages: therapeutic approaches in cancer. *Nat Rev*  
914 *Drug Discov* **17**, 887-904, doi:10.1038/nrd.2018.169 (2018).
- 915 13 Lopez-Yrigoyen, M., Cassetta, L. & Pollard, J. W. Macrophage targeting in cancer. *Ann NY Acad Sci*  
916 **1499**, 18-41, doi:10.1111/nyas.14377 (2021).
- 917 14 Pathria, P., Louis, T. L. & Varner, J. A. Targeting Tumor-Associated Macrophages in Cancer. *Trends*  
918 *Immunol* **40**, 310-327, doi:10.1016/j.it.2019.02.003 (2019).
- 919 15 Beatty, G. L. *et al.* CD40 agonists alter tumor stroma and show efficacy against pancreatic  
920 carcinoma in mice and humans. *Science* **331**, 1612-1616, doi:10.1126/science.1198443 (2011).
- 921 16 Cannarile, M. A. *et al.* Colony-stimulating factor 1 receptor (CSF1R) inhibitors in cancer therapy. *J*  
922 *Immunother Cancer* **5**, 53, doi:10.1186/s40425-017-0257-y (2017).
- 923 17 Chaib, M., Chauhan, S. C. & Makowski, L. Friend or Foe? Recent Strategies to Target Myeloid Cells  
924 in Cancer. *Front Cell Dev Biol* **8**, 351, doi:10.3389/fcell.2020.00351 (2020).
- 925 18 Hu, J. *et al.* Regulation of tumor immune suppression and cancer cell survival by CXCL1/2 elevation  
926 in glioblastoma multiforme. *Sci Adv* **7**, doi:10.1126/sciadv.abc2511 (2021).
- 927 19 Logtenberg, M. E. W., Scheeren, F. A. & Schumacher, T. N. The CD47-SIRPalpha Immune  
928 Checkpoint. *Immunity* **52**, 742-752, doi:10.1016/j.immuni.2020.04.011 (2020).
- 929 20 Veillette, A. & Chen, J. SIRPalpha-CD47 Immune Checkpoint Blockade in Anticancer Therapy.  
930 *Trends Immunol* **39**, 173-184, doi:10.1016/j.it.2017.12.005 (2018).
- 931 21 Bassler, K., Schulte-Schrepping, J., Warnat-Herresthal, S., Aschenbrenner, A. C. & Schultze, J. L.  
932 The Myeloid Cell Compartment-Cell by Cell. *Annu Rev Immunol* **37**, 269-293,  
933 doi:10.1146/annurev-immunol-042718-041728 (2019).

- 934 22 Gosselin, D. *et al.* An environment-dependent transcriptional network specifies human microglia  
935 identity. *Science* **356**, doi:10.1126/science.aal3222 (2017).
- 936 23 Zhang, L. *et al.* Single-Cell Analyses Inform Mechanisms of Myeloid-Targeted Therapies in Colon  
937 Cancer. *Cell* **181**, 442-459 e429, doi:10.1016/j.cell.2020.03.048 (2020).
- 938 24 Muller, S. *et al.* Single-cell profiling of human gliomas reveals macrophage ontogeny as a basis for  
939 regional differences in macrophage activation in the tumor microenvironment. *Genome Biol* **18**,  
940 234, doi:10.1186/s13059-017-1362-4 (2017).
- 941 25 Jordao, M. J. C. *et al.* Single-cell profiling identifies myeloid cell subsets with distinct fates during  
942 neuroinflammation. *Science* **363**, doi:10.1126/science.aat7554 (2019).
- 943 26 Alvarez-Errico, D., Vento-Tormo, R., Sieweke, M. & Ballestar, E. Epigenetic control of myeloid cell  
944 differentiation, identity and function. *Nat Rev Immunol* **15**, 7-17, doi:10.1038/nri3777 (2015).
- 945 27 Chen, L. *et al.* Genetic Drivers of Epigenetic and Transcriptional Variation in Human Immune Cells.  
946 *Cell* **167**, 1398-1414 e1324, doi:10.1016/j.cell.2016.10.026 (2016).
- 947 28 De Leo, A., Ugolini, A. & Veglia, F. Myeloid Cells in Glioblastoma Microenvironment. *Cells* **10**,  
948 doi:10.3390/cells10010018 (2020).
- 949 29 Locarno, C. V. *et al.* Role of myeloid cells in the immunosuppressive microenvironment in gliomas.  
950 *Immunobiology* **225**, 151853, doi:10.1016/j.imbio.2019.10.002 (2020).
- 951 30 Preusser, M., Lim, M., Hafler, D. A., Reardon, D. A. & Sampson, J. H. Prospects of immune  
952 checkpoint modulators in the treatment of glioblastoma. *Nat Rev Neurol* **11**, 504-514,  
953 doi:10.1038/nrneurol.2015.139 (2015).
- 954 31 Andersen, B. M. *et al.* Glial and myeloid heterogeneity in the brain tumour microenvironment.  
955 *Nat Rev Cancer* **21**, 786-802, doi:10.1038/s41568-021-00397-3 (2021).
- 956 32 Goswami, S. *et al.* Immune profiling of human tumors identifies CD73 as a combinatorial target in  
957 glioblastoma. *Nat Med* **26**, 39-46, doi:10.1038/s41591-019-0694-x (2020).
- 958 33 Xiang, Y. *et al.* JMJD3 is a histone H3K27 demethylase. *Cell Res* **17**, 850-857,  
959 doi:10.1038/cr.2007.83 (2007).
- 960 34 Croker, B. A. *et al.* SOCS3 negatively regulates IL-6 signaling in vivo. *Nat Immunol* **4**, 540-545,  
961 doi:10.1038/ni931 (2003).
- 962 35 Kim, H. & Seed, B. The transcription factor MafB antagonizes antiviral responses by blocking  
963 recruitment of coactivators to the transcription factor IRF3. *Nat Immunol* **11**, 743-750,  
964 doi:10.1038/ni.1897 (2010).
- 965 36 Zhang, X. *et al.* Macrophage/microglial Ezh2 facilitates autoimmune inflammation through  
966 inhibition of Socs3. *J Exp Med* **215**, 1365-1382, doi:10.1084/jem.20171417 (2018).
- 967 37 Neftel, C. *et al.* An Integrative Model of Cellular States, Plasticity, and Genetics for Glioblastoma.  
968 *Cell* **178**, 835-849 e821, doi:10.1016/j.cell.2019.06.024 (2019).
- 969 38 Wei, R. *et al.* Spatial charting of single-cell transcriptomes in tissues. *Nat Biotechnol* **40**, 1190-  
970 1199, doi:10.1038/s41587-022-01233-1 (2022).
- 971 39 Abram, C. L., Roberge, G. L., Hu, Y. & Lowell, C. A. Comparative analysis of the efficiency and  
972 specificity of myeloid-Cre deleting strains using ROSA-EYFP reporter mice. *J Immunol Methods*  
973 **408**, 89-100, doi:10.1016/j.jim.2014.05.009 (2014).
- 974 40 Shi, J., Hua, L., Harmer, D., Li, P. & Ren, G. Cre Driver Mice Targeting Macrophages. *Methods Mol*  
975 *Biol* **1784**, 263-275, doi:10.1007/978-1-4939-7837-3\_24 (2018).
- 976 41 Swiecki, M. & Colonna, M. The multifaceted biology of plasmacytoid dendritic cells. *Nat Rev*  
977 *Immunol* **15**, 471-485, doi:10.1038/nri3865 (2015).
- 978 42 Kedl, R. M. *et al.* Migratory dendritic cells acquire and present lymphatic endothelial cell-archived  
979 antigens during lymph node contraction. *Nat Commun* **8**, 2034, doi:10.1038/s41467-017-02247-z  
980 (2017).

- 981 43 Salmon, H. *et al.* Expansion and Activation of CD103(+) Dendritic Cell Progenitors at the Tumor  
982 Site Enhances Tumor Responses to Therapeutic PD-L1 and BRAF Inhibition. *Immunity* **44**, 924-938,  
983 doi:10.1016/j.immuni.2016.03.012 (2016).
- 984 44 Overwijk, W. W. *et al.* Tumor regression and autoimmunity after reversal of a functionally tolerant  
985 state of self-reactive CD8+ T cells. *J Exp Med* **198**, 569-580, doi:10.1084/jem.20030590 (2003).
- 986 45 Hashizume, R. *et al.* Pharmacologic inhibition of histone demethylation as a therapy for pediatric  
987 brainstem glioma. *Nat Med* **20**, 1394-1396, doi:10.1038/nm.3716 (2014).
- 988 46 Li, Y. *et al.* Therapeutic potential of GSK-J4, a histone demethylase KDM6B/JMJD3 inhibitor, for  
989 acute myeloid leukemia. *J Cancer Res Clin Oncol* **144**, 1065-1077, doi:10.1007/s00432-018-2631-  
990 7 (2018).
- 991 47 Sui, A. *et al.* The pharmacological role of histone demethylase JMJD3 inhibitor GSK-J4 on glioma  
992 cells. *Oncotarget* **8**, 68591-68598, doi:10.18632/oncotarget.19793 (2017).
- 993 48 Liu, T. M., Wang, H., Zhang, D. N. & Zhu, G. Z. Transcription Factor MafB Suppresses Type I  
994 Interferon Production by CD14(+) Monocytes in Patients With Chronic Hepatitis C. *Front Microbiol*  
995 **10**, 1814, doi:10.3389/fmicb.2019.01814 (2019).
- 996 49 Motohashi, H. & Igarashi, K. MafB as a type I interferon rheostat. *Nat Immunol* **11**, 695-696,  
997 doi:10.1038/ni0810-695 (2010).
- 998 50 Kershaw, N. J. *et al.* SOCS3 binds specific receptor-JAK complexes to control cytokine signaling by  
999 direct kinase inhibition. *Nat Struct Mol Biol* **20**, 469-476, doi:10.1038/nsmb.2519 (2013).
- 1000 51 Donahoe, R. M. & Huang, K. Y. Interferon preparations enhance phagocytosis in vivo. *Infect Immun*  
1001 **13**, 1250-1257, doi:10.1128/iai.13.4.1250-1257.1976 (1976).
- 1002 52 Gottfried-Blackmore, A. *et al.* Acute in vivo exposure to interferon-gamma enables resident brain  
1003 dendritic cells to become effective antigen presenting cells. *Proc Natl Acad Sci U S A* **106**, 20918-  
1004 20923, doi:10.1073/pnas.0911509106 (2009).
- 1005 53 Wong, G. H., Clark-Lewis, I., McKimm-Breschkin, L., Harris, A. W. & Schrader, J. W. Interferon-  
1006 gamma induces enhanced expression of Ia and H-2 antigens on B lymphoid, macrophage, and  
1007 myeloid cell lines. *J Immunol* **131**, 788-793 (1983).
- 1008 54 Barrat, F. J., Crow, M. K. & Ivashkiv, L. B. Interferon target-gene expression and epigenomic  
1009 signatures in health and disease. *Nat Immunol* **20**, 1574-1583, doi:10.1038/s41590-019-0466-2  
1010 (2019).
- 1011 55 Feng, M. *et al.* Phagocytosis checkpoints as new targets for cancer immunotherapy. *Nat Rev*  
1012 *Cancer* **19**, 568-586, doi:10.1038/s41568-019-0183-z (2019).
- 1013 56 Liu, X. *et al.* CD47 blockade triggers T cell-mediated destruction of immunogenic tumors. *Nat Med*  
1014 **21**, 1209-1215, doi:10.1038/nm.3931 (2015).
- 1015 57 Clausen, B. E., Burkhardt, C., Reith, W., Renkawitz, R. & Forster, I. Conditional gene targeting in  
1016 macrophages and granulocytes using LysMcre mice. *Transgenic Res* **8**, 265-277,  
1017 doi:10.1023/a:1008942828960 (1999).
- 1018 58 McGinnis, C. S., Murrow, L. M. & Gartner, Z. J. DoubletFinder: Doublet Detection in Single-Cell  
1019 RNA Sequencing Data Using Artificial Nearest Neighbors. *Cell Syst* **8**, 329-337 e324,  
1020 doi:10.1016/j.cels.2019.03.003 (2019).
- 1021 59 Stuart, T. *et al.* Comprehensive Integration of Single-Cell Data. *Cell* **177**, 1888-1902 e1821,  
1022 doi:10.1016/j.cell.2019.05.031 (2019).
- 1023 60 Satpathy, A. T. *et al.* Massively parallel single-cell chromatin landscapes of human immune cell  
1024 development and intratumoral T cell exhaustion. *Nat Biotechnol* **37**, 925-936,  
1025 doi:10.1038/s41587-019-0206-z (2019).
- 1026 61 Pliner, H. A. *et al.* Cicero Predicts cis-Regulatory DNA Interactions from Single-Cell Chromatin  
1027 Accessibility Data. *Mol Cell* **71**, 858-871 e858, doi:10.1016/j.molcel.2018.06.044 (2018).



- 1028 62 Langmead, B. & Salzberg, S. L. Fast gapped-read alignment with Bowtie 2. *Nat Methods* **9**, 357-  
1029 359, doi:10.1038/nmeth.1923 (2012).
- 1030 63 Faust, G. G. & Hall, I. M. SAMBLASTER: fast duplicate marking and structural variant read  
1031 extraction. *Bioinformatics* **30**, 2503-2505, doi:10.1093/bioinformatics/btu314 (2014).
- 1032 64 Li, H. *et al.* The Sequence Alignment/Map format and SAMtools. *Bioinformatics* **25**, 2078-2079,  
1033 doi:10.1093/bioinformatics/btp352 (2009).
- 1034 65 Tarasov, A., Vilella, A. J., Cuppen, E., Nijman, I. J. & Prins, P. Sambamba: fast processing of NGS  
1035 alignment formats. *Bioinformatics* **31**, 2032-2034, doi:10.1093/bioinformatics/btv098 (2015).
- 1036 66 Zhang, Y. *et al.* Model-based analysis of ChIP-Seq (MACS). *Genome Biol* **9**, R137, doi:10.1186/gb-  
1037 2008-9-9-r137 (2008).
- 1038 67 Yu, G., Wang, L. G. & He, Q. Y. ChIPseeker: an R/Bioconductor package for ChIP peak annotation,  
1039 comparison and visualization. *Bioinformatics* **31**, 2382-2383, doi:10.1093/bioinformatics/btv145  
1040 (2015).
- 1041 68 Wu, T. *et al.* clusterProfiler 4.0: A universal enrichment tool for interpreting omics data.  
1042 *Innovation (Camb)* **2**, 100141, doi:10.1016/j.xinn.2021.100141 (2021).
- 1043 69 Shao, Z., Zhang, Y., Yuan, G. C., Orkin, S. H. & Waxman, D. J. MAnorm: a robust model for  
1044 quantitative comparison of ChIP-Seq data sets. *Genome Biol* **13**, R16, doi:10.1186/gb-2012-13-3-  
1045 r16 (2012).
- 1046 70 Ramirez, F. *et al.* deepTools2: a next generation web server for deep-sequencing data analysis.  
1047 *Nucleic Acids Res* **44**, W160-165, doi:10.1093/nar/gkw257 (2016).
- 1048 71 Lerdrup, M., Johansen, J. V., Agrawal-Singh, S. & Hansen, K. An interactive environment for agile  
1049 analysis and visualization of ChIP-sequencing data. *Nat Struct Mol Biol* **23**, 349-357,  
1050 doi:10.1038/nsmb.3180 (2016).
- 1051 72 Nowicka, M. *et al.* CyTOF workflow: differential discovery in high-throughput high-dimensional  
1052 cytometry datasets. *F1000Res* **6**, 748, doi:10.12688/f1000research.11622.2 (2017).

1053

1054

1055

1056

1057

1058

1059

1060

1061

1062 **Acknowledgment**

1063 This research is supported by the MD Anderson Physician Scientist Award (S.G), Khalifa  
1064 Physician Scientist Award (S.G), Andrew Sabin Family Foundation Fellows Award (S.G) and  
1065 Clinic and Laboratory Integration Program Award (S.G). We acknowledge Liangwen Xiong,  
1066 Baoxiang Guan, Derek Ng Tang, Sydney Kemp and Alison Jung for technical assistance. We  
1067 acknowledge the CATALYST-working group at MD Anderson Cancer Center for human GBM  
1068 tumor samples. CATALYST is supported by the MD Anderson GBM Moon Shot™. Dr. Sharma is  
1069 a member of the Parker Institute for Cancer Immunotherapy.

1070

1071 **Author information**

1072 S.G. developed the project, designed the experiments, analyzed data, wrote the manuscript and  
1073 acquired funding. D.R, S.M.N, P.S performed the experiments, analyzed data and wrote the  
1074 manuscript. Y.C, performed bioinformatics analyses. J.Z, M.H, S.A helped with the murine  
1075 experiments. B.P.K, C.P and F.L provided human GBM tumor samples. M.M and S.J performed  
1076 the H&E, IHC and IF staining of human GBM samples. S.B and Z.H helped with the human  
1077 scRNA-sequencing and VISIUM analysis. P.S oversaw the study, provided scientific input, edited  
1078 the manuscript and acquired funding.

1079

1080 **Ethics declarations**

1081 Competing interest

1082 P.S. reports consulting, advisory roles, and/or stocks/ownership for Achelois, Apricity Health,  
1083 BioAlta, Codiak BioSciences, Constellation, Dragonfly Therapeutics, Forty-Seven Inc.,  
1084 Hummingbird, ImaginAb, Jounce Therapeutics, Lava Therapeutics, Lytix Biopharma, Marker

1085 Therapeutics, BioNTx, Oncolytics, Glympse, Infinity Pharma, and Polaris and owns a patent

1086 licensed to Jounce Therapeutics.

1087

1088

1089

1090

1091

1092

1093

1094

1095

1096

1097

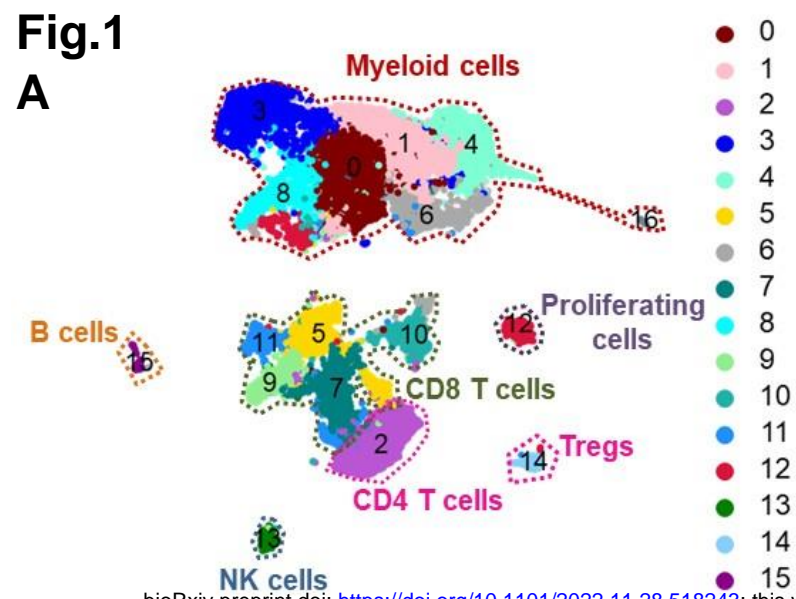
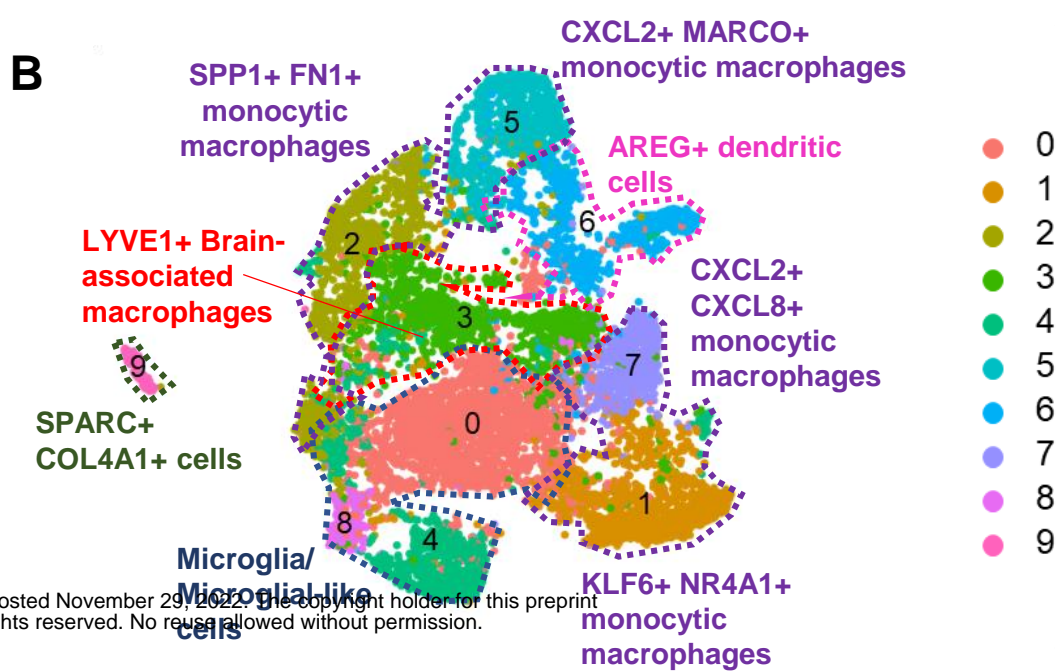
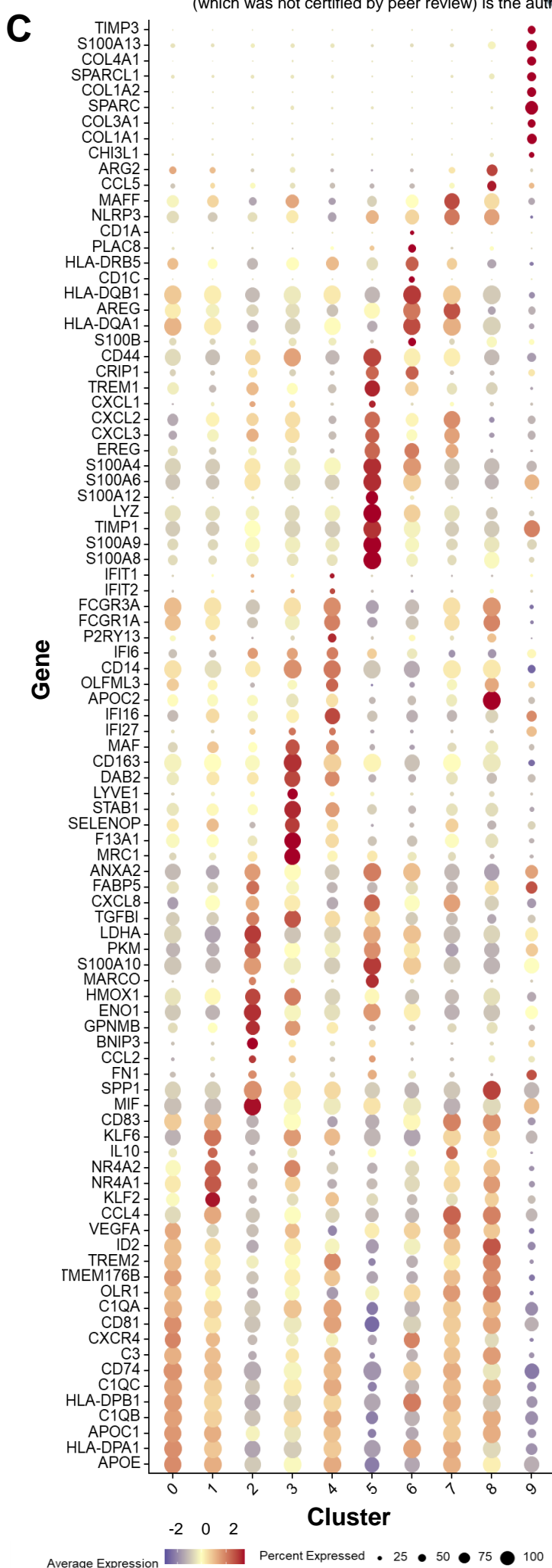
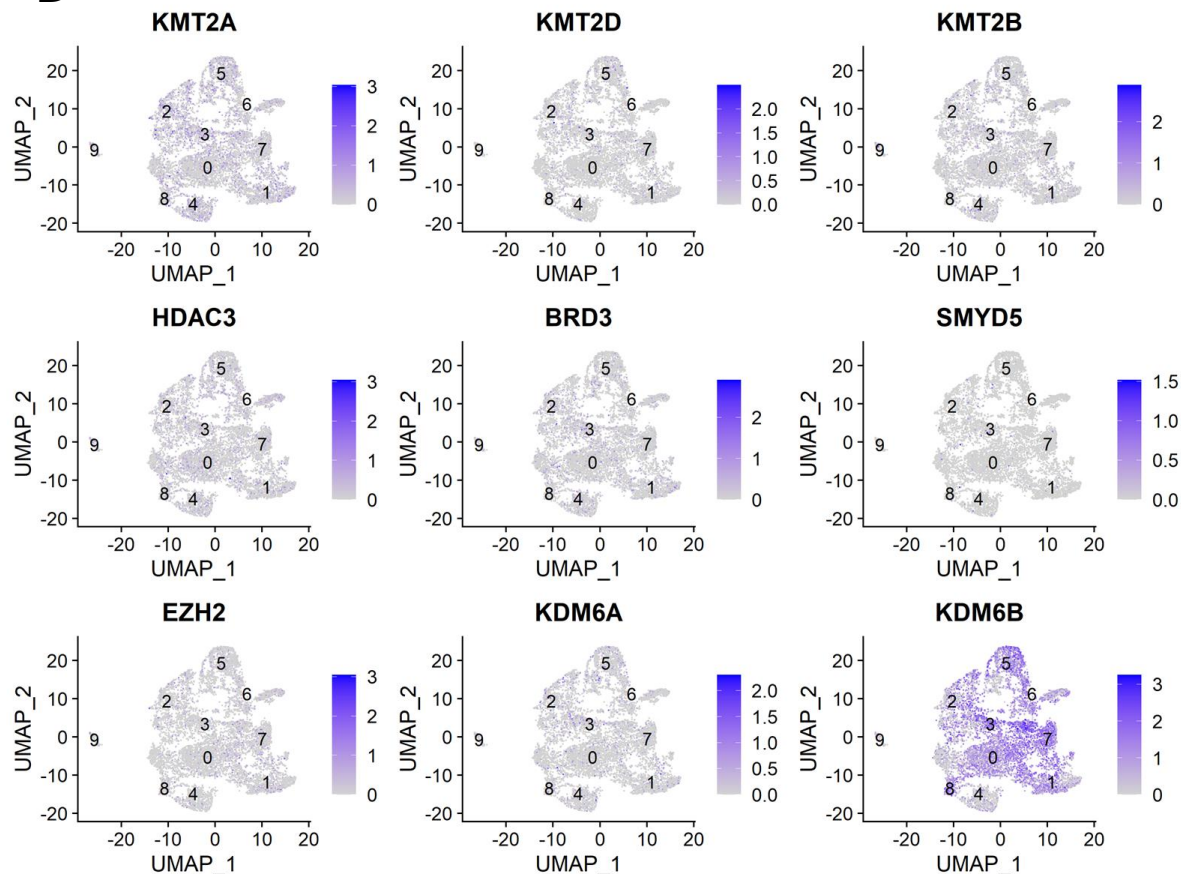
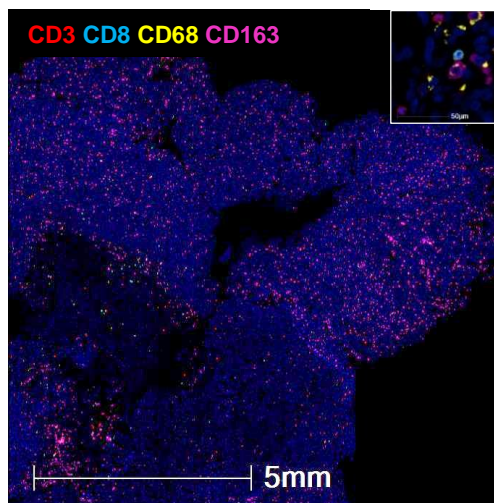
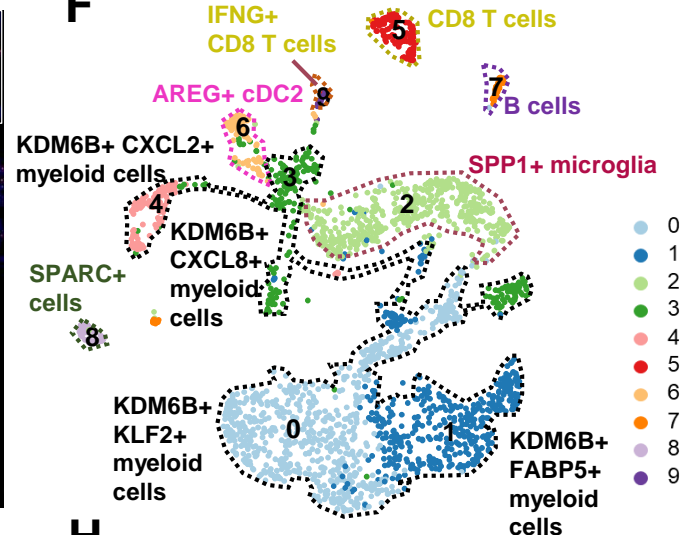
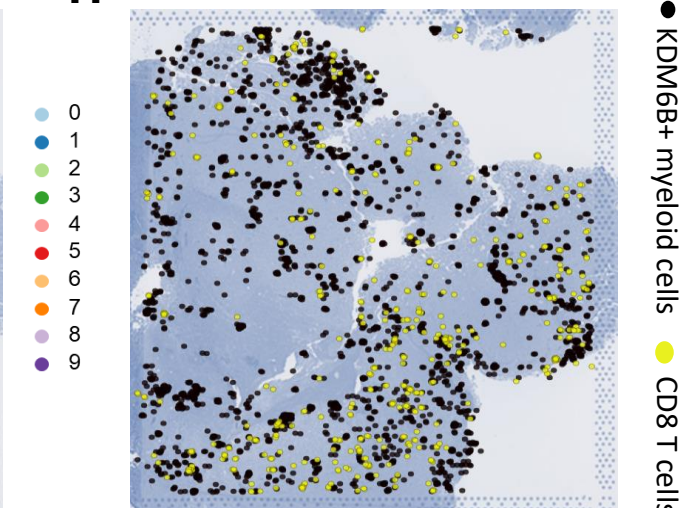
1098

1099

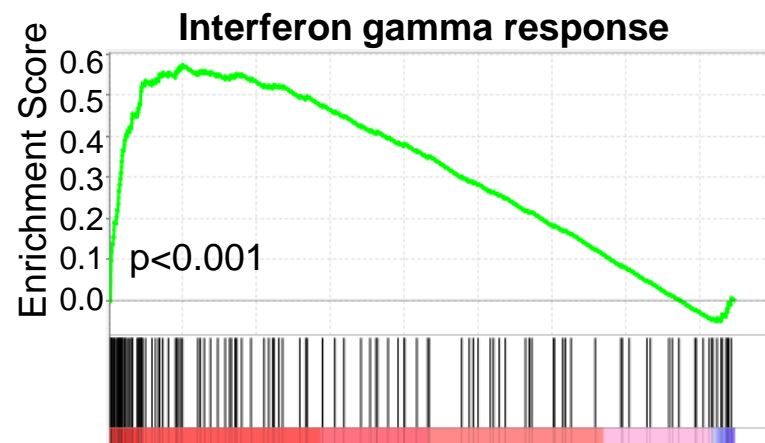
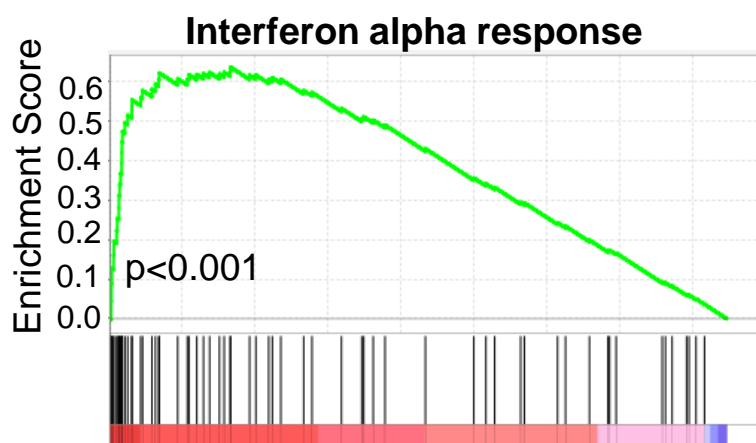
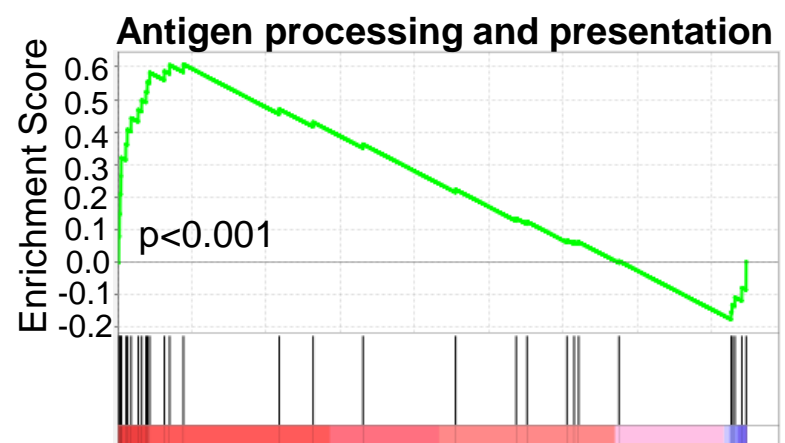
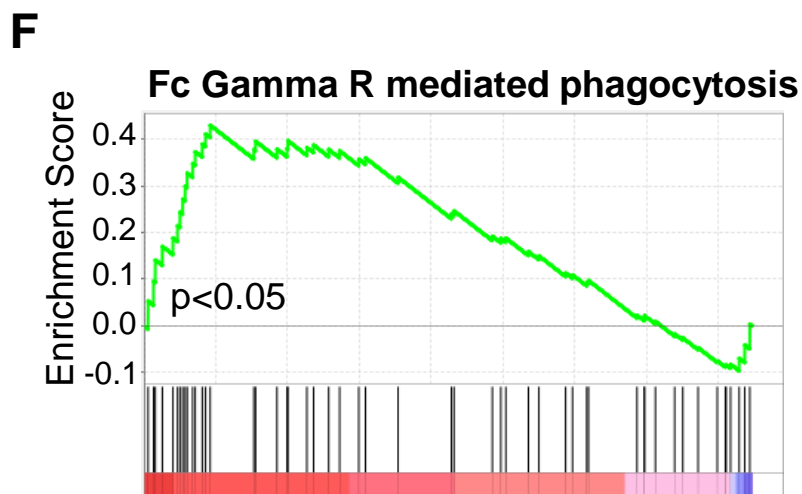
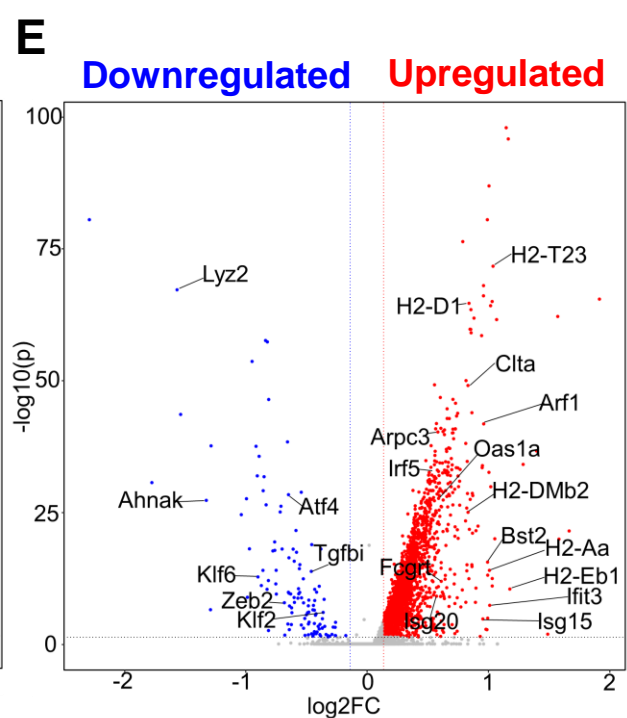
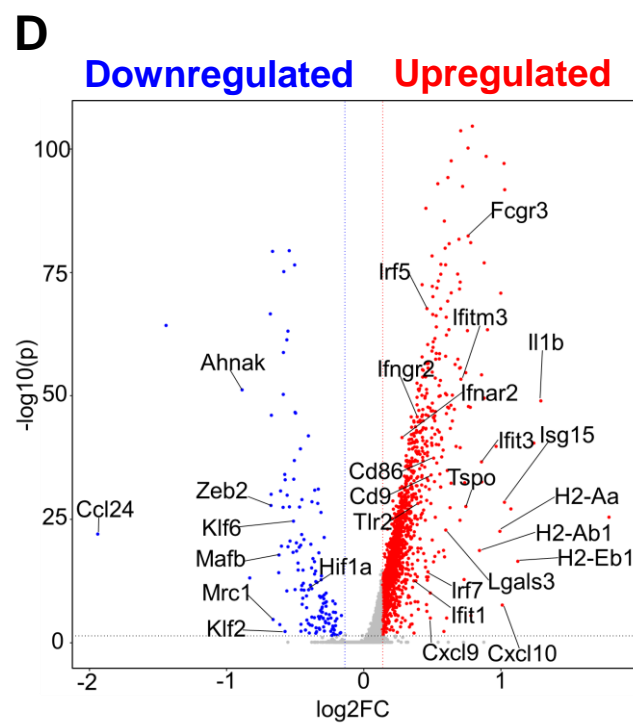
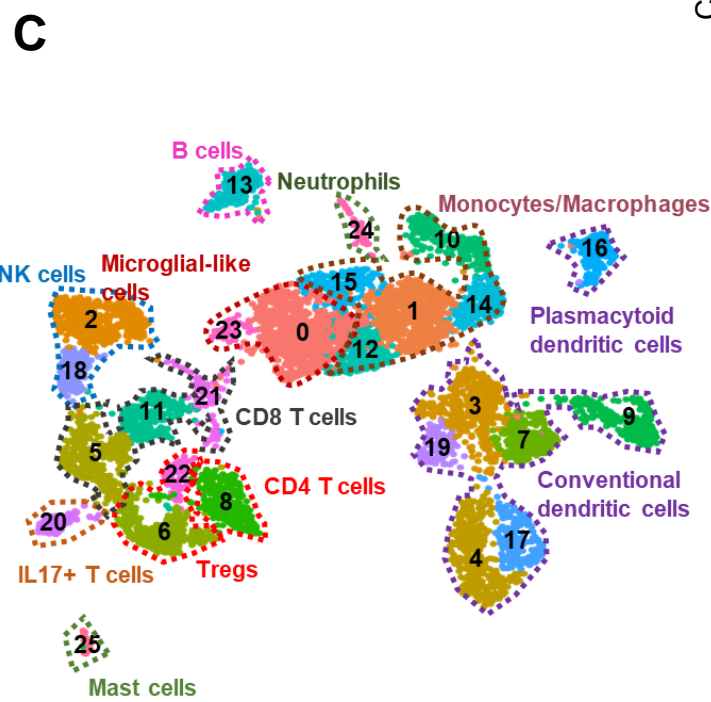
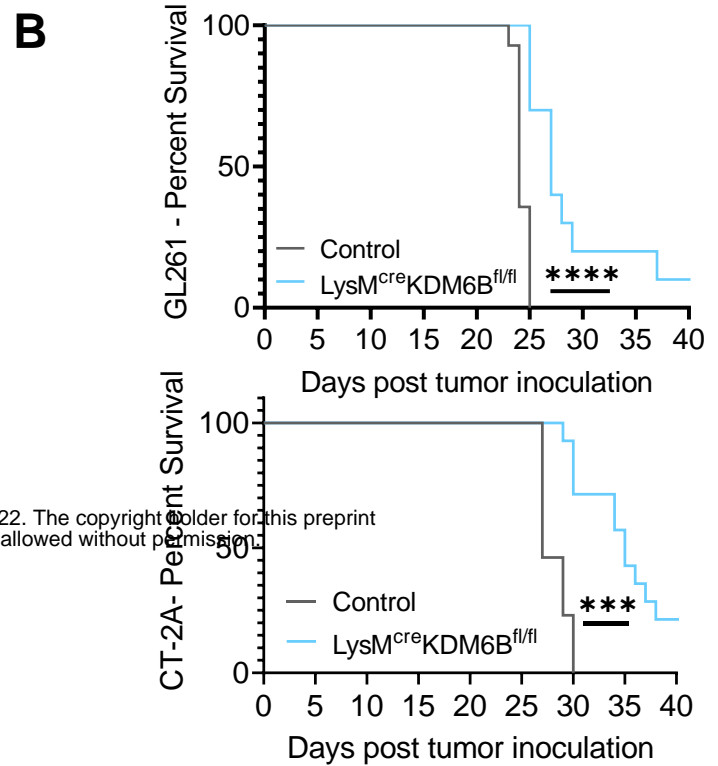
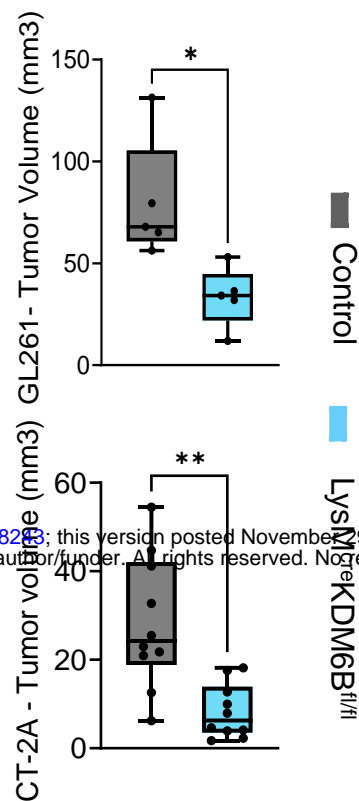
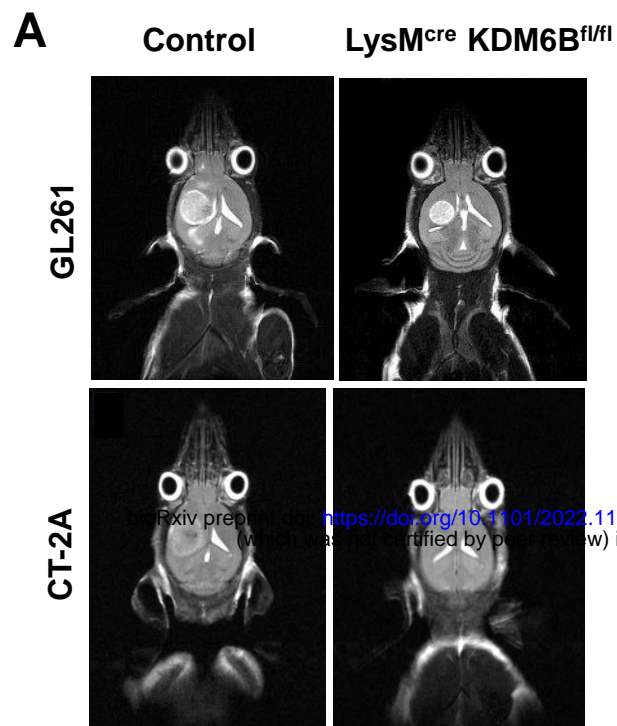
1100

1101

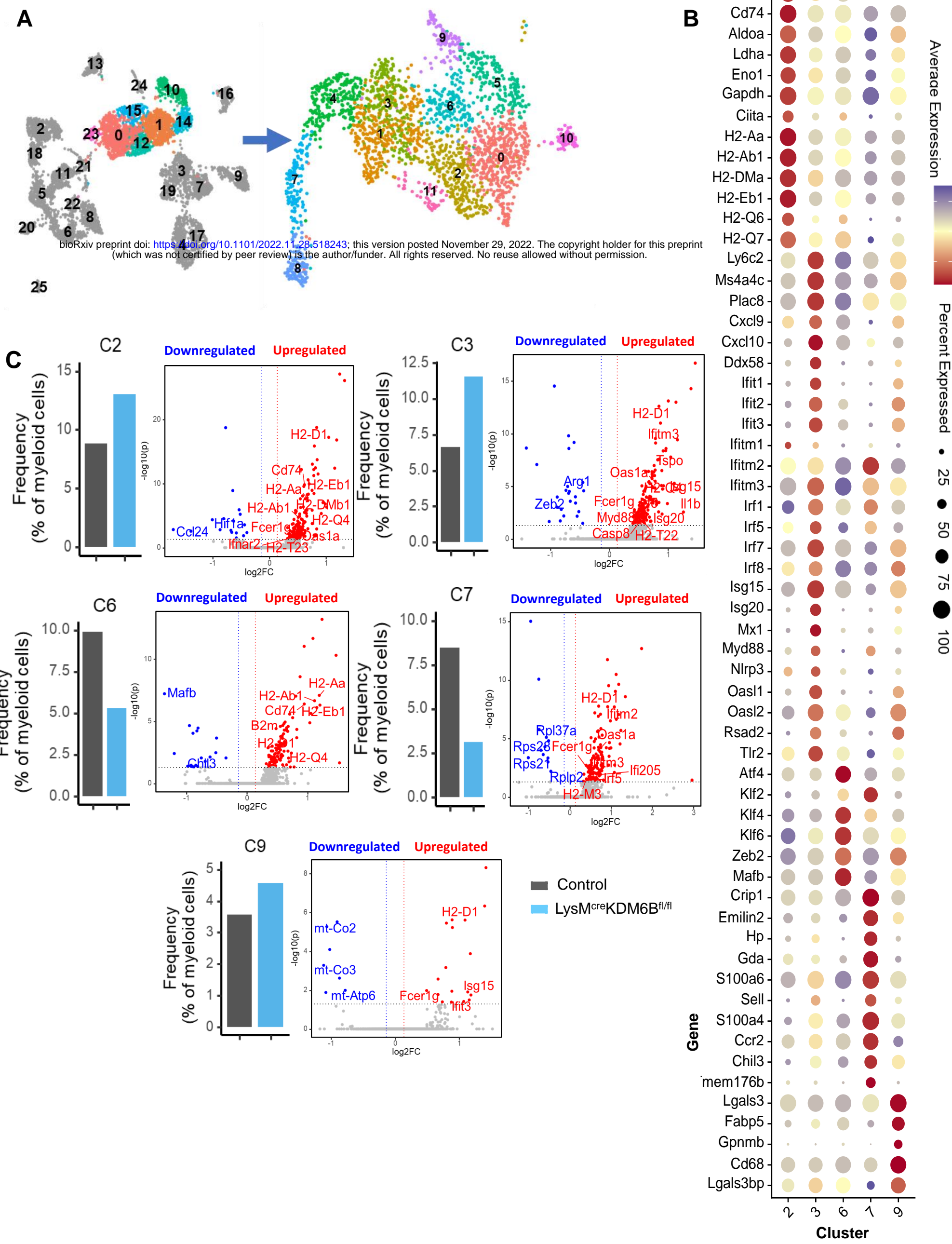
1102

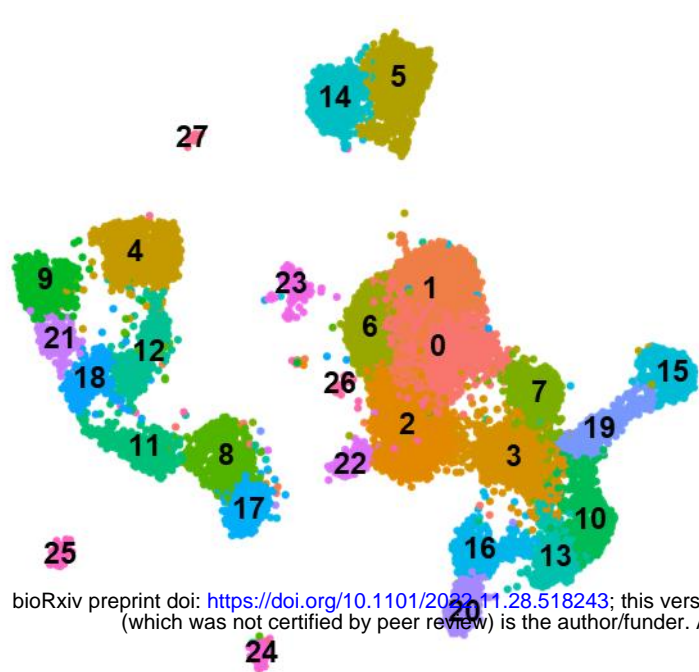
**Fig.1****A****B****C****D****E****F****G****H**

bioRxiv preprint doi: <https://doi.org/10.1101/2022.11.28.518243>; this version posted November 29, 2022. The copyright holder for this preprint (which was not certified by peer review) is the author/funder. All rights reserved. No reuse allowed without permission.

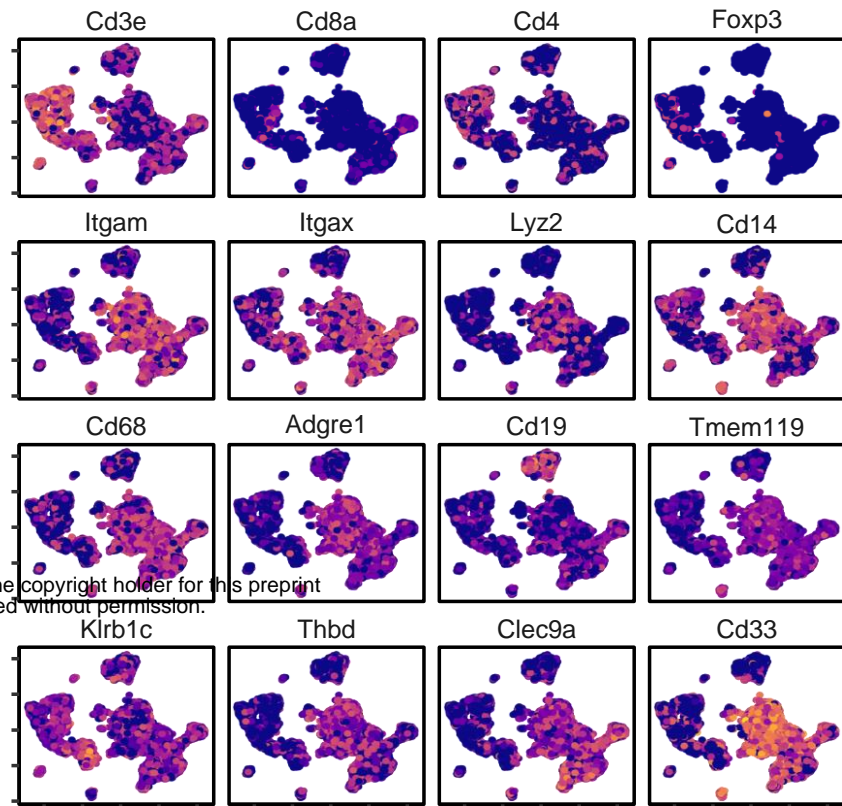
**Fig. 2**

**Fig. 3**

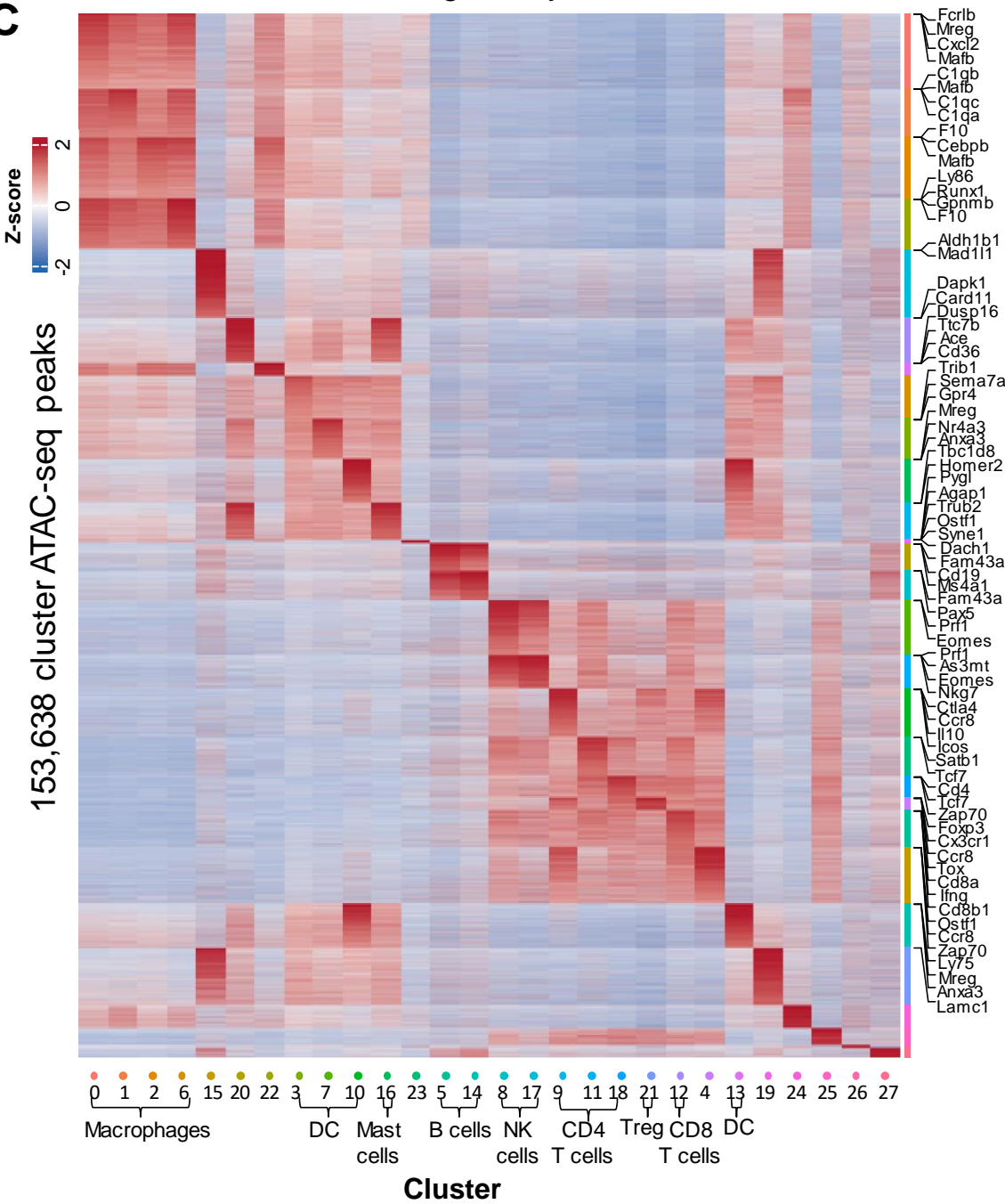
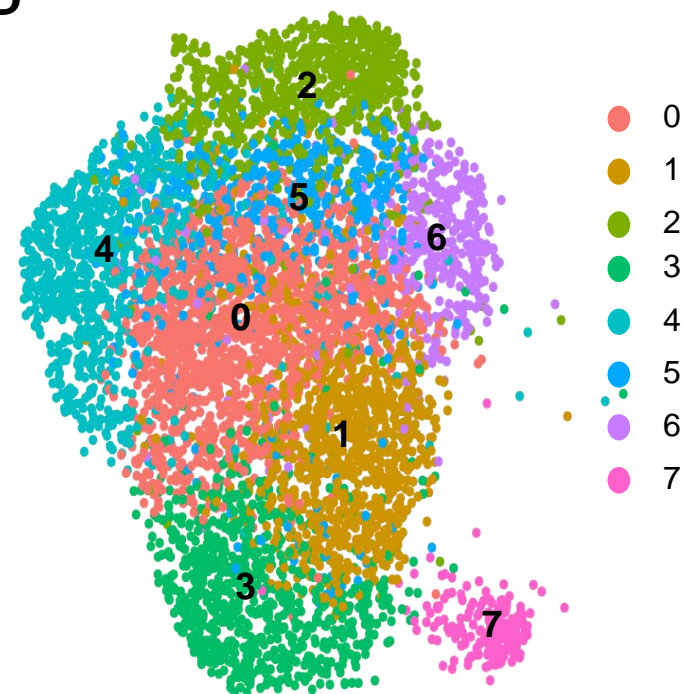
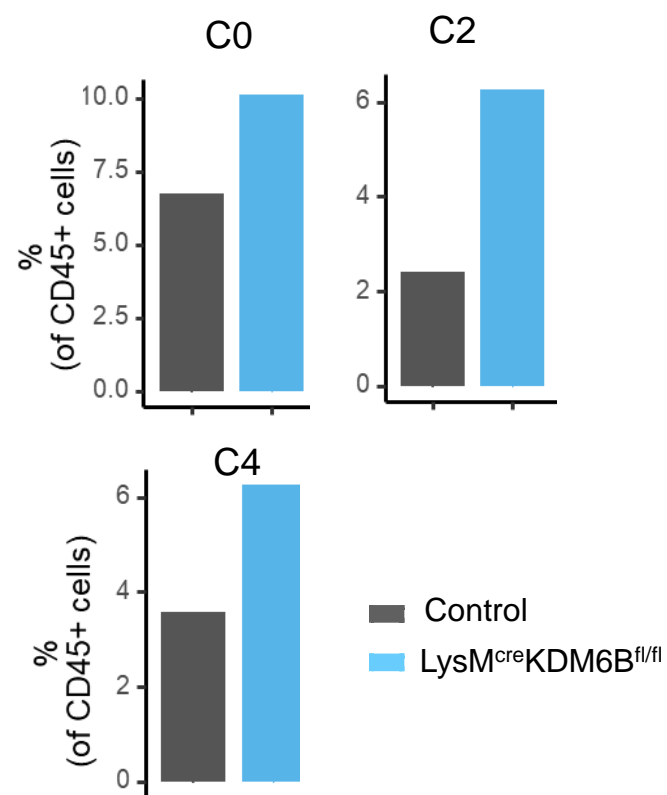
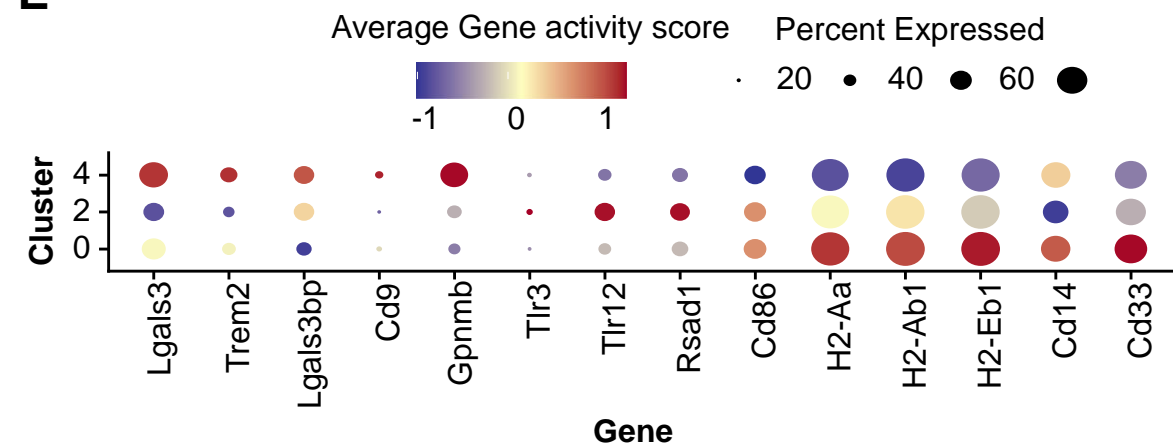


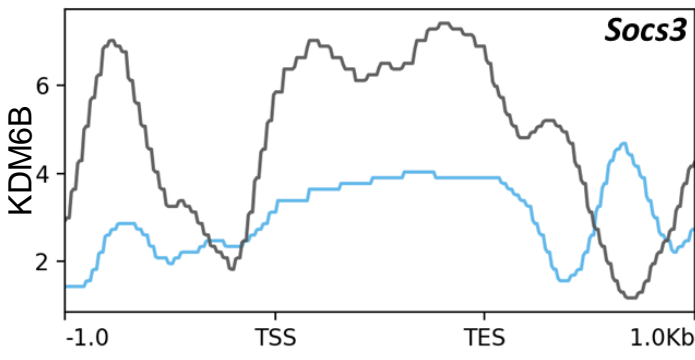
**Fig.4****A**

bioRxiv preprint doi: <https://doi.org/10.1101/2022.11.28.518243>; this version posted November 29, 2022. The copyright holder for this preprint (which was not certified by peer review) is the author/funder. All rights reserved. No reuse allowed without permission.

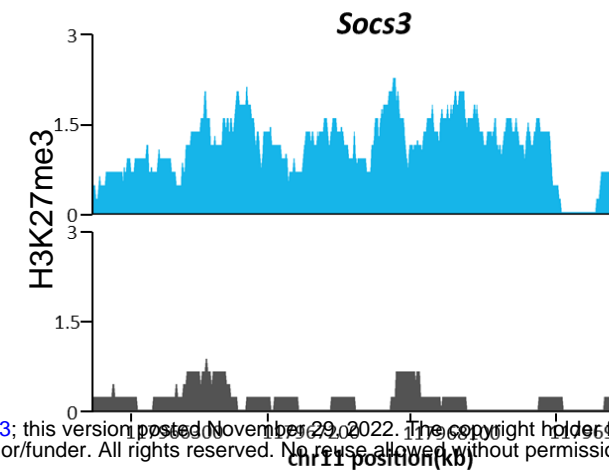
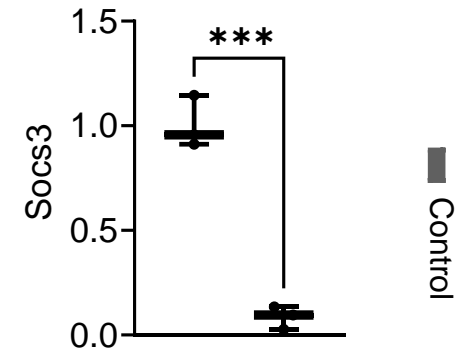
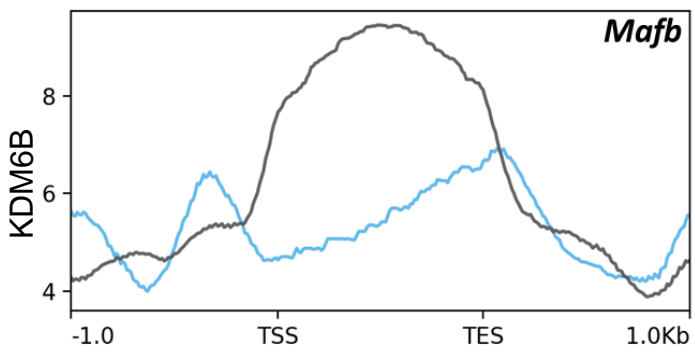
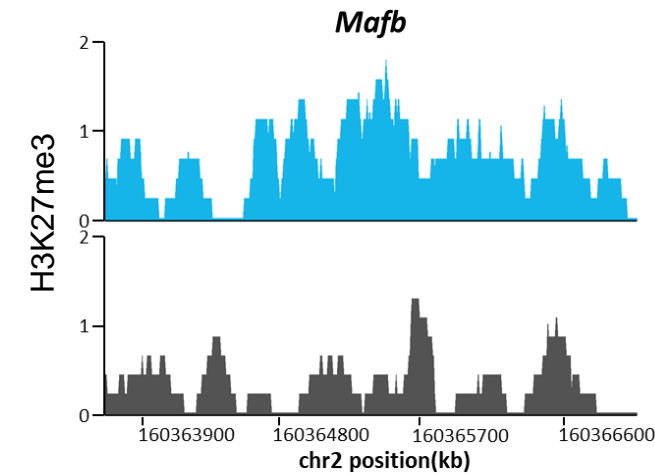
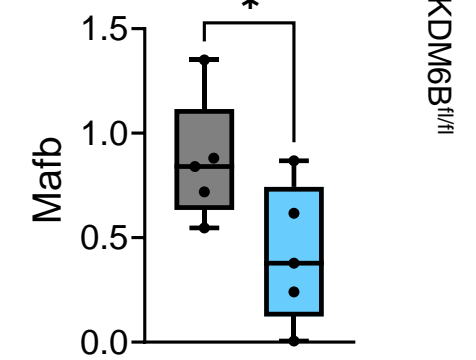
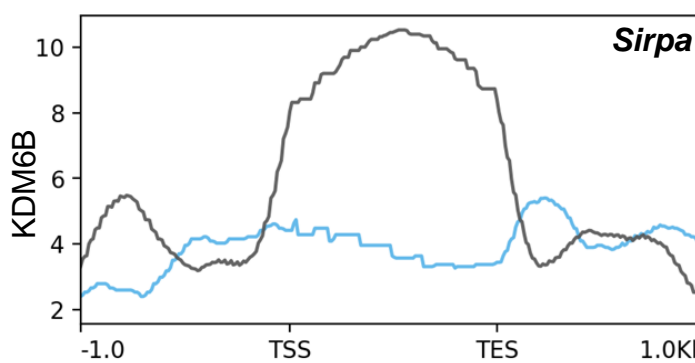
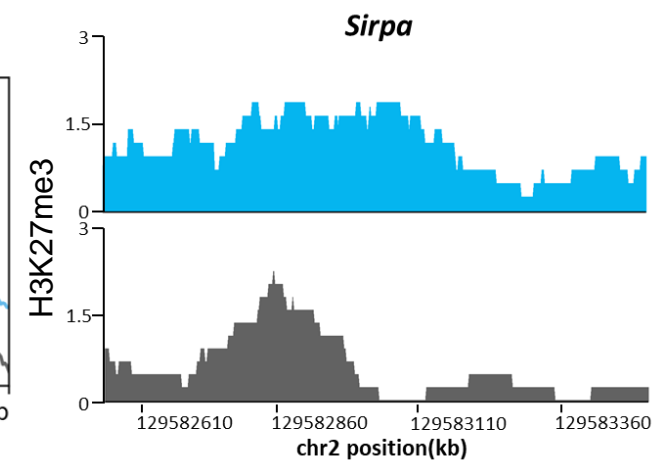
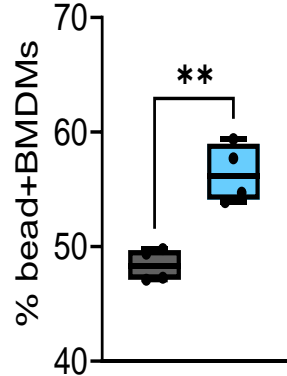
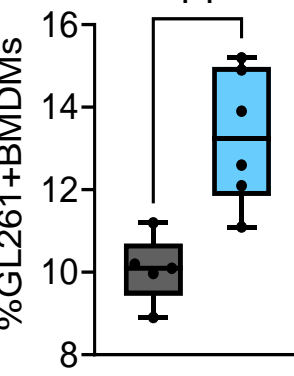
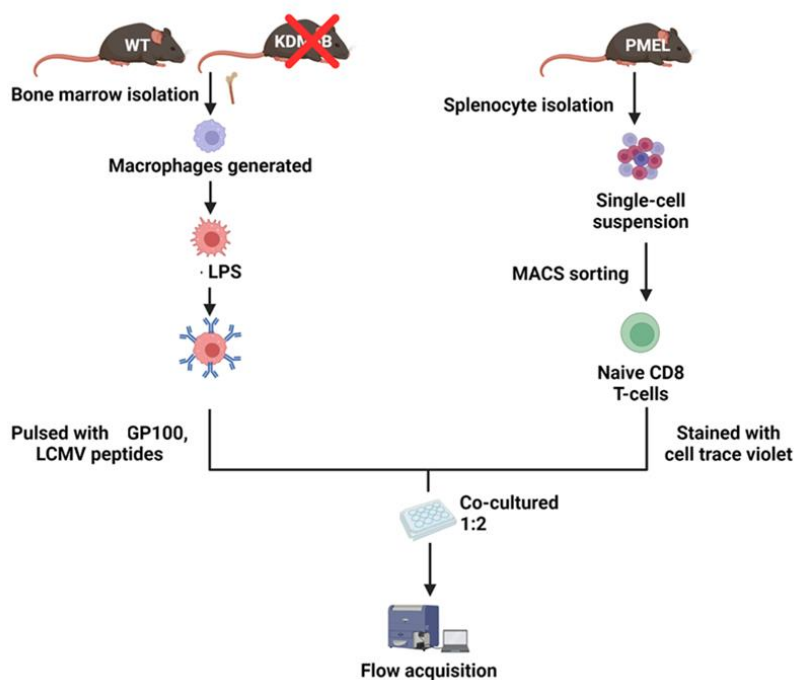
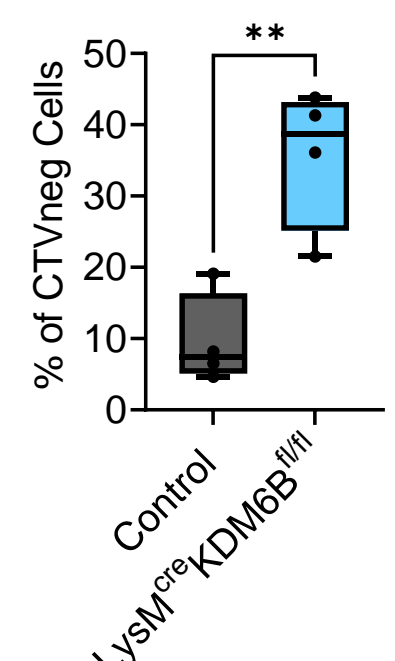
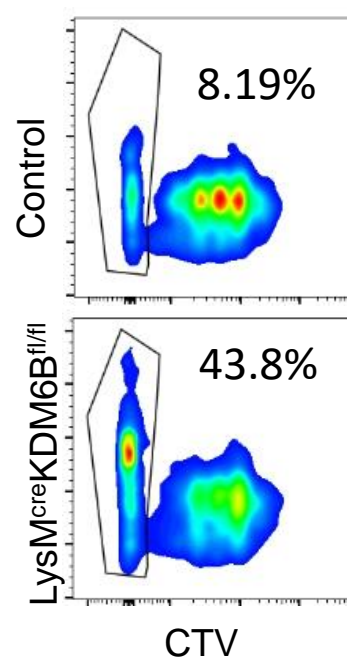
**B****C**

Cis-regulatory elements

**D****F****E**

**Fig. 5****A**

bioRxiv preprint doi: <https://doi.org/10.1101/2022.11.28.518243>; this version posted November 29, 2022. The copyright holder for this preprint (which was not certified by peer review) is the author/funder. All rights reserved. No reuse allowed without permission.

**B****C****D****E****F****G****H****I****J****K****L**



**Fig. 6**